Time-, tissue- and treatment-associated heterogeneity in tumour-residing migratory DCs

Colin YC Lee[1,2], Bethany C Kennedy[3], Nathan Richoz[1], Zewen K Tuong[1,2], Isaac Dean[3], Fabrina Gaspal[3], Zhi Li[3], Claire Willis[3], Tetsuo Hasegawa[1], Sarah K Whiteside[4], David A Posner[1], Gianluca Carlesso[5], Scott A Hammond[5], Simon J Dovedi[6], Rahul Roychoudhuri[4], David R Withers[3#], Menna R Clatworthy[1,2#]

[1] Molecular Immunity Unit, Department of Medicine, Medical Research Council Laboratory of Molecular Biology, University of Cambridge, Cambridge, UK

[2] Cellular Genetics, Wellcome Sanger Institute, Wellcome Genome Campus, Hinxton, Cambridge, UK

[3] Institute of Immunology and Immunotherapy, College of Medical and Dental Sciences, University of Birmingham, Birmingham, UK

[4] Department of Pathology, University of Cambridge, Cambridge, UK

[5] Early Oncology R&D, AstraZeneca, Gaithersburg, USA

[6] Early Oncology R&D, AstraZeneca, Cambridge, UK

[#] **Correspondence:**
Prof. David R Withers, D.Withers@bham.ac.uk;
Prof. Menna R Clatworthy, mrc38@medschl.cam.ac.uk

Abstract

CCR7-expressing mature DCs enriched in immunoregulatory molecules (mRegDCs), such as PD-L1, have been identified in tumours and draining lymph nodes (dLN), but their spatiotemporal dynamics and role in anti-tumour immune responses remain unclear. Using photoconvertible mice to precisely track DC migration, we found that mRegDCs comprised the dominant DC population arriving in the dLN, but a subset remained tumour-resident despite CCR7 expression. These tumour-retained mRegDCs were phenotypically and transcriptionally distinct from their dLN counterparts and were heterogeneous, with increasing features of an "exhausted" transcriptional profile with more prolonged tumour residence. This was characterised by reduced expression of antigen presentation and pro-inflammatory transcripts, and these "exhaustion" features were attenuated by anti-PD-L1 treatment. Tumour mRegDCs spatially co-localised with effector $CD8^+$ T cells in human solid tumours, and anti-PD-L1 treatment enhanced their expression of several T cell-stimulatory molecules. Altogether, these data provide fundamental insights into mRegDC biology and their role in cancer immunotherapy.

Introduction

Dendritic cells (DCs) capture tumour antigens and upregulate the chemokine receptor CCR7, which directs their migration to secondary lymphoid organs where they present antigens to T cells[1–3]. Two major conventional DC (cDC) subsets have been identified in tumours; cDC1 that specialise in cross-presenting tumour antigens to $CD8^+$ T cells and are associated with improved survival[4], and cDC2 that present exogenous antigen to $CD4^+$ T cells and have variable associations with cancer prognosis and treatment responses[1]. The recent application of single-cell technologies to tissue samples has enabled the distinction of an intratumoral DC population that may arise from both cDC1 and cDC2, but demonstrates a conserved phenotype and transcriptional programme characterised by the expression of LAMP3, genes consistent with a mature and migratory state (CCR7, CD40, IL12), and immunoregulatory molecules including PD-L1 and PD-L2[5]. This DC subset or state has been variously labelled as "migratory DCs", "mature DCs enriched in immunoregulatory molecules" (mRegDCs, the term we adopted in the current study), as well as "$LAMP3^+$ DCs", or cDC3[6]. Regardless of nomenclature, single-cell atlasing efforts have identified mRegDCs in multiple human cancers[7–9], and the acquisition of this transcriptional programme appears dependent on the phagocytic receptor AXL and uptake of tumour antigens[5].

Intriguingly, despite the conserved expression of co-inhibitory molecules such as PD-L1 in mRegDCs, the expression of the mRegDC-associated marker LAMP3 is associated with improved prognosis in breast, lung cancer and metastatic melanoma[10–13]. However, the precise contribution of mRegDCs to anti-tumour responses, and whether they have a positive or negative effect on disease outcomes remains unclear. Certainly, mRegDCs are likely to be key targets of immune checkpoint blockade (ICB) by virtue of their high expression of co-inhibitory molecules. Consistent with this, murine studies demonstrate the importance of DC-expressed PD-L1 in determining anti-tumour cytotoxic responses to subcutaneously tumours[14–16], and the application of anti-IL4 to increase mRegDCs enhanced responses to anti-PD-L1 in a non-small cell lung cancer (NSCLC) model[5].

mRegDCs express high levels of CCR7, enabling trafficking from the tumour to draining lymph nodes (dLN)[5,17]. Indeed, $LAMP3^+$ DCs have been identified in tumour-dLN, where they may activate tumour antigen-specific T cells[18]. However, LAMP3-expressing DCs have also been described within tertiary lymphoid structures in tumours[13,19], suggesting that some mature DCs may be retained in tumours for prolonged periods. Thus, the precise temporal dynamic behaviour of mRegDCs, the extent to which they act within the tumour versus dLN, and how these dynamics and site-specific cellular interactions are influenced by ICB remain to be clarified. The concept that prolonged residence within tumours might influence mRegDC fate and function is worthy of consideration given the known effects of the tumour microenvironment (TME) on other immune cell populations. For example, $CD8^+$ T cells transition to a so-called 'exhausted' state with prolonged dwell time in the tumour[20], with three defining characteristics; reduced effector function, sustained expression of inhibitory molecules such as PD-1, and a transcriptional state distinct from that of functional effector cells[21]. These features have also been observed in other tumour-resident immune cells such as natural killer (NK) cells[22,23].

Here, we used a photo-tracking mouse model, combined with single-cell RNA sequencing (scRNA-seq), confocal imaging and spatial transcriptomics, in mouse and human tissues, to interrogate the spatio-temporal dynamics of mRegDCs, their roles within the tumour, and the effects of ICB. We found mRegDCs showed transcriptional heterogeneity, influenced by duration of tumour residence, location (tumour versus dLN), and anti-PDL1 treatment. Strikingly, tumour-retained mRegDCs showed similar expression of CCR7 to those that migrated the dLN but took on an increasingly "exhausted" transcriptional profile with more prolonged tumour dwell time. These intratumoural mRegDCs co-localised with cytotoxic $CD8^+$ T cells, and anti-PD-L1 treatment enhanced their expression of several

77 important T cell-stimulatory molecules. mRegDC-CD8$^+$ T cell engagement and their augmentation by
78 ICB was confirmed across a range of human cancers. Altogether, these data provide further insight to
79 tumour mRegDC dynamics and their role in ICB therapy.
80

Results

mRegDC signatures are associated with improved survival in human cancers

The presence of mature LAMP$^+$ DCs within lymphoid follicles has been associated with improved prognosis in NSCLC[10], but the effect of tumour mRegDCs on prognosis in human cancers more broadly has not been examined. To address this, we analysed the transcriptomes of 4,045 human solid tumours from the cancer genome atlas (TCGA)[24]. Enrichment of an mRegDC signature was associated with improved survival not only in lung cancer, but also in cutaneous melanoma, breast, and colorectal cancer (CRC, **Supplementary Fig. 1A**), all of which harbour CCR7$^+$ mRegDCs (**Supplementary Fig. 1B-G**)[25–27]. Further analysis of 1,853 human breast tumours from METABRIC[28] revealed cancer subtype-specific prognostic associations (**Supplementary Fig. 1H**). These data suggest that mRegDCs contribute to anti-tumour responses across a range of human cancers.

mRegDCs are transcriptionally heterogenous, and some subpopulations remain within the tumour despite CCR7 expression

To investigate the mechanisms by which mRegDCs promote anti-tumour immunity, we sought to characterise their spatio-temporal dynamics. The mRegDC programme is thought to be driven by acquisition of tumour antigen[5]. We asked whether establishment of this programme inevitably leads to the trafficking of CCR7$^+$ mRegDCs to the dLN, or whether some cells remain in the tumour. To address this, we established multiple syngeneic subcutaneous colorectal tumours (MC38, CT26) in a photoconvertible Kaede transgenic model that enables site-specific temporal labelling of cells within the tumour[29]**.** Tumours were transcutaneously photoconverted on day 13, converting infiltrating cells from the default green fluorescence (Kaede-green) to a red fluorescent profile (Kaede-red)[20]. 24-72h following photo-conversion, tumours were harvested, enabling the distinction of newly infiltrating Kaede-green cells from tumour-retained Kaede-red cells (**Fig. 1A**). To address the effect of ICB on mRegDC dynamics, we administered anti-PD-L1 antibodies in this model (**Supplementary Fig. 2A**), selecting this target because mRegDCs in CRC showed the highest expression of PD-L1 among immune cells (**Supplementary Fig. 1C**).

scRNA-seq of FACS-isolated Kaede-green$^+$ or Kaede-red$^+$ myeloid cells (CD45$^+$Ter119$^-$ CD11b$^+$NK1.1$^-$), as well as tumour-infiltrating lymphocytes (TIL, CD45$^+$Ter119$^-$CD11b$^-$) isolated 48h after photoconversion (**Supplementary Fig. 2B**) generated 80,556 single cell transcriptomes following rigorous quality control, including 32,191 myeloid cells (**Fig. 1B**, **Supplementary Fig. 2C**). Unbiased clustering of DCs revealed 8 distinct clusters, including cycling DCs, cDC1, cDC2s, and mRegDCs, assigned based on expression of canonical marker genes and similarity to published transcriptomes (**Fig. 1C-D**, **Supplementary Fig. 2D**), with mRegDC showing high expression of *Ccr7*, *Cd274* and *Pdcd1lg2*. Indeed, mRegDCs expressed higher levels of surface PD-L1 than other immune cells (**Supplementary Fig. 2E-F**).

Over 50% of tumour DCs were mRegDC, and surprisingly, they were predominantly Kaede-red (**Fig. 1E**, **Supplementary Fig. 2G**). In contrast, cDC1 and cDC2 were mostly Kaede-green, consistent with the conclusion that these newly infiltrating cDCs differentiate into mRegDCs following uptake of tumour antigen[5]. The majority of mRegDCs expressed IRF8, consistent with a cDC1 origin, with a smaller number expressing the cDC2-associated IRF4 (**Fig. 1D**). The prevalence of Kaede-red mRegDCs was validated by flow cytometry in both MC38 and CT26 subcutaneous tumours (**Fig. 1F**, **Supplementary Fig. 2H-J**), where mRegDCs were the major Kaede-red DC cell-type at 24h, 48h and 72h post-photoconversion (**Fig. 1G**). Finally, we confirmed the presence of Kaede-red MHC-II$^+$CCR7$^+$ cells by immunofluorescence (IF) microscopy (**Fig. 1H**, **Supplementary Fig. 3A-B**).

To explore the relationship between tumour cDC subsets, we performed a pseudotime analysis rooted in the Kaede-green dominant cluster (cDC2_1). This revealed a trajectory terminating in mRegDC_2/3 that transitioned through the mRegDC_1 state (**Fig. 1I**, **Supplementary Fig. 3C**), consistent with the Kaede-green/red ratio of clusters that marks tumour dwell in real time. Kaede-red^{+} cDC1 and cDC2 showed higher expression of migratory transcripts and *Ciita*, a master regulator of antigen presentation[30], than Kaede-green^{+} counterparts, suggesting that cDCs mature with duration in the TME (**Supplementary Fig. 3D**). Principal component (PC) analysis showed that Kaede status (green versus red) accounted for approximately 70% of the transcriptional variance in cDC2s (PC1, **Supplementary Fig. 3E**). Genes driving PC1 were enriched in pathways relating to antigen presentation and myeloid differentiation (**Supplementary Fig. 3F**). cDC2_3, the cDC cluster with most Kaede-red cells, upregulated *Ciita*, class-II MHC (MHC-II) transcripts, and *Ccr7* compared with cDC2_2 (**Supplementary Fig. 3H**). The receptor tyrosine kinase *Axl*, which induces the mRegDC programme[5], was also upregulated as cDC2_1 transitioned to cDC2_3 (**Figure 1J**). Altogether, these data suggest time-associated maturation of cDCs in the TME towards an mRegDC state and that antigen-charged mRegDCs may reside in the tumour for several days, despite the expression of genes involved in tumour egress, including CCR7.

Migrated mRegDCs are transcriptionally distinct from tumour-residing mRegDCs

DCs expressing mRegDC transcripts have been identified in tumour-dLN[5,31], but given our demonstration that mRegDCs in tumours represent the dominant Kaede-red long-dwelling DC population, we sought to definitively track tumour DC egress to dLNs. Kaede-red DCs originating from the tumour were readily detectable in the dLN, but not in the contralateral non-draining LN (ndLN), and were CCR7^{+}PD-L2^{+}MHC-II^{high} (**Fig. 2A-B**). Kaede-red mRegDCs comprised a stable population across time, making up 30% of mRegDCs in the dLN at 24h, 48h and 72h post-photoconversion (**Fig. 2C**). scRNA-seq of sorted Kaede-red CD45^{+} cells from tumour-dLNs, and CD45^{+} cells from control LNs included a prominent *Ccr7*$^{+}$*Cd274*$^{+}$ cluster assigned as mRegDCs (**Fig. 2D**, **Supplementary Fig. 4A-B**). In this data, 94% of Kaede-red^{+} myeloid cells in the dLN were mRegDCs (**Fig. 2E**), placing them as the dominant myeloid cell tumour emigrants arriving in the dLN.

Compared to Kaede-red tumour emigrants in the dLN, mRegDCs in tumour were enriched in '*interferon gamma response*' genes (**Fig. 2F**). There was no difference in mRegDC '*lymphocyte co-stimulation*' geneset expression between sites, but the precise co-stimulatory molecules differed (**Fig. 2F**, **Supplementary Fig. 4B-C**). Specifically, CD80 and CD86 were higher in tumour mRegDCs, confirmed at a protein level, while *Icosl* (ICOS ligand) was significantly higher in dLN mRegDCs (**Fig. 2G-H**). Of note, CD80/86 and ICOSL have differing effects on T cell activation, where signalling through CD28 but not ICOS induces IL-2 production to support the clonal expansion of T cells[32]. *Il12b*, which drives anti-tumour cytotoxic T cell activity[33], was enriched in tumour mRegDCs, while *Il15ra*, a marker of DC maturation[34], was higher in mRegDC in the dLN. Re-analysis of scRNA-seq from B16-F10 tumours and their dLN[35] confirmed tissue-associated heterogeneity in mRegDCs (**Supplementary Fig. 4D-G**).

We next asked whether the three transcriptionally distinct tumour mRegDC subsets contributed equally to the dLN emigrants. To address this, we integrated the single-cell transcriptomes of tumour-originating DCs in the dLN with the tumour DC landscape (**Fig. 2I**). Strikingly, 80% of Kaede-red DCs from the dLN mapped to the tumour mRegDC_1 cluster (**Fig. 2J**). Only 9% of DCs in the dLN were mRegDC_2/3, despite mRegDC_2/3 being the dominant Kaede-red^{+} tumour mRegDC subsets. Although *Ccr7* expression remained high throughout mRegDC_1, 2 and 3, we observed a decrease in transcripts associated with DC chemotaxis and CCR7 signalling in mRegDC_2 and 3 (**Supplementary Fig. 4H-I**).

171 These data suggest that mRegDC_1, which have most recently acquired the mRegDC programme, are
172 the main population to seed the dLN. Hence, we propose that mRegDC_2 and mRegDC_3 are terminal,
173 tumour-residing mRegDC states, and DCs that have transited through the intermediate mRegDC_1
174 state, become increasingly unlikely to egress.

175 **Tumour-retained mRegDCs progress towards an "exhausted" state**

176 Since tumour-residing mRegDC subsets are reduced in their migratory capacity, we sought to assess
177 how their transcriptional programmes changed across pseudotime with longer tumour dwell-time.
178 During the transition from mRegDC_1 to mRegDC_2, there was upregulation of *Il12b*, *Cd80*, *Cd40*
179 (**Supplementary Fig. 5A)** potentially augmenting their capacity to promote anti-tumour responses.
180 However, with further pseudotime progression, we observed a decrease in MHC-II expression in
181 mRegDC_2/3, including class-II invariant chain *Cd74*, (**Fig. 3A**, **Supplementary Fig. 5B**). Similarly,
182 DC antigen presentation genes decreased as cells transitioned towards the tumour-retained
183 mRegDC_2/3 states (**Fig. 3B-C**). This included downregulation of molecules involved in antigen
184 processing (*Ctsb*, *Ctsl*, *Ifi30*, *Lgmn*, *Psme2*), transport (*Tap1*, *Tap2*), chaperones (*Hsp1a1*, *Hspa2*,
185 *Hspa8*), MHC loading (*H2-DMa*, *H2-Oa*, *Tapbp*, *Calr*) and *Ciita* (**Supplementary Fig. 5C-D**).

186 Moreover, genes involved in several important immunological processes, including '*interferon gamma*
187 *response*', '*inflammatory response*' and '*cytokine-cytokine receptor signalling*' pathway genes,
188 significantly decreased as cells transitioned from the mRegDC_1 to mRegDC_3 states (**Fig. 3D**).
189 mRegDC_3 showed reduced expression of several innate immune genes (*Nlrp3*, *Tlr1*, *Cd14*), genes
190 involved in DC activation and migration (*Axl*, *Ccr7*, *Rgs1*, *Icam1*), lymphocyte co-stimulation (*Cd40*,
191 *Tnfsf9*, *Pvr*) and cytokines which may recruit and activate immune cells (*Cxcl9*, *Il1b*, *Tnf*) compared
192 with mRegDC1 (**Fig. 3E**, **Supplementary Fig. 5E**). Hence, mRegDCs retained in the tumour undergo
193 a transition, acquiring the transcriptional hallmarks of "exhaustion", as defined in T cells, namely
194 reduced expression of molecules enabling effector function (in this case, antigen presentation),
195 sustained expression of inhibitory molecules, and a transcriptional state distinct from that of functional
196 effector cells[21].

197 **mRegDCs interact with CD8 T cells in human tumours**

198 Given that a substantial proportion of mRegDCs in tumour failed to migrate to dLN, and that tumour
199 mRegDCs may associate with outcomes, we sought to identify which immune cells mRegDCs may
200 communicate within the tumour. We deconvolved 521 human CRC transcriptomes[24] and found the
201 highest correlation between mRegDC and $CD8^+$ T cell transcripts (**Fig. 4A**), an observation replicated
202 in melanoma, breast, and lung tumour biopsies (**Fig. 4B**). Furthermore, the
203 *CCR7*$^+$*CD274*$^+$*PDCD1LG2*$^+$ DC cluster (consistent with mRegDCs in human CRC[27])
204 (**Supplementary Fig. 1B-C**), had stronger predicted interactions with effector $CD8^+$ T cells than other
205 myeloid cells, including via CD28, CTLA-4 and PD-1 (*PDCD1*) engagement (**Fig. 4C**). Similar
206 observations were confirmed in scRNA-seq of human breast tumours and melanoma (**Supplementary**
207 **Fig. 1D-G**)[25,26].

208 Effective engagement of cell-surface ligand-receptor pairs requires co-localisation of mRegDCs and
209 effector $CD8^+$ T cells. Analysis of spatial transcriptomics data from human CRC tumours[36] revealed
210 hotspots with co-localised expression of mRegDC and effector $CD8^+$ T cell genes (**Fig. 4D-E**,

Supplementary Fig. 5F). Spatial correlation of mRegDC and effector CD8$^+$ T cell transcripts was also evident in breast tumours and melanoma (**Supplementary Fig. 5G-H**).

Finally, we analysed data from RNA-seq of physically-interacting cells (PICs), consisting of sorted myeloid-T cell doublets from NSCLC[37]. Of note, mRegDC-T cell PICs were more frequent in tumours than normal tissue[37]. We found that mRegDC-CD8$^+$ T cell doublets were more frequent than other mRegDC-T cell combinations (**Supplementary Fig. 5I-J**), and PICs containing mRegDC (*CCR7$^+$FSCN1$^+$CD274$^+$*) highly co-expressed *CD8B, PRF1, GZMB and PDCD1* (**Fig. 4F**), confirming that in NSCLC, mRegDC and effector CD8$^+$ T cells physically interact.

Altogether, these data suggest that mRegDC-CD8$^+$ T cell interaction is conserved across multiple human solid tumours. These interactions may regulate T cell activation and could be important targets in cancer immunotherapy.

Anti-PD-L1 reduces the abundance of tumour mRegDCs with an 'exhaustion-like' state and promotes CD8$^+$ T cell interactions

Loss of PD-L1 expression from host immune cells, not tumour cells, is an important driver of inflammatory gene expression in the TME (**Supplementary Fig. 6A**), so we investigated the effects of anti-PD-L1 treatment on tumour DCs. In cDC2s, anti-PD-L1 treatment led to the upregulation genes involved in inflammation and adaptive immunity and an increased expression of *Axl* expression as cDC2_1 transitioned to cDC2_3 (**Supplementary Fig. 3G-I**). Across all mRegDC subsets, similar pathways were enriched following anti-PD-L1, including "*interferon gamma response*", necessary for effective response to ICB[33], and "*antigen processing and presentation*" genes were upregulated in mRegDC_1 (**Supplementary Fig. 6B-C**).

Assessment of differential abundance[38] showed a significant enrichment in cellular neighbourhoods of mRegDC_2 following anti-PD-L1 treatment, but a relative depletion of mRegDC_3 (**Fig. 5A**). Strikingly, mRegDC_2 was highly transcriptionally activated compared to mRegDC_3, including marked upregulation of many transcripts involved in immune signalling, such as *Cd40*, *Fos*, *Nfkbia*, *Tnf*, etc. (**Fig. 5B**). These collectively drove enrichment in multiple gene signatures relating to immune activation, such as TNF and cytokine signalling (**Supplementary Fig. 6D**). Importantly, we identified several ligands that were differentially expressed on mRegDC_2 compared to other tumour mRegDC subsets, and also relative to mRegDCs in the dLN, including *Il12b*, *Tnfsf4*, *Tnfsf9*, *Cd70* and *Pvr* (**Supplementary Fig. 6E-F**). These molecules have established roles in supporting T cell activation[33,39,40] and were also preferentially expressed on tumour-residing mRegDCs in B16-F10 tumours (**Supplementary Fig. 4G**). These data suggest that an "activated" tumour-residing mRegDC state is enriched following anti-PD-L1 treatment.

To investigate the effects of anti-PD-L1 on mRegDC-CD8 T cell interactions in tumour, we analysed scRNA-seq of TILs (**Supplementary Fig. 2B**, **7A-B**), identifying a *Prf1$^+$Gzm$^+$Pdcd1$^+$Havcr2$^+$* CD8$^+$ T cell cluster resembling "exhausted" T (T_{EX}) cells[41,42] (**Fig. 5C**, **Supplementary Fig. 7C-D**) that were predominantly tumour-resident and expanded with anti-PD-L1 (**Fig. 5D**, **Supplementary Fig. 7E**). T_{EX} cells were evident among the cycling_CD8T cluster and increased in proliferation following anti-PD-L1, potentially underpinning their increased number (**Supplementary Fig. 7F-I**). Among CD8 T cells, the T_{EX} cells also showed the largest transcriptional response to anti-PD-L1 (**Fig. 5E**), including upregulation of genes involved in "*T cell receptor signalling*" and "*TNFα signalling via NFκB*", with potential beneficial anti-tumour effects (**Supplementary Fig. 7J**). Indeed, Kaede-red$^+$PD-1$^+$ CD8$^+$ T cells showed a significant increase in Granzyme B and IFNγ protein expression (**Supplementary Fig. 7H**,**K-L**).

255 Since mRegDCs are the major source of PD-L1 in tumours, and CD8$^+$ T_{EX} cells the primary responders
256 to anti-PD-L1 therapy, we interrogated the molecular interactions between these two cell types that
257 might promote CD8$^+$ T_{EX} activation and proliferation post-anti-PD-L1 using ligand-receptor expression
258 analysis[43] (**Fig. 5F**). This revealed several previously described interactions, including *CXCL16* and
259 *IL15* from CCR7$^+$ DCs which may recruit and sustain cytotoxic T cells (**Supplementary Fig. 8A**)[44].
260 mRegDC_3 had fewer activating interactions with CD8$^+$ T_{EX} cells than mRegDC_1/2, supporting their
261 status as an "exhausted" mRegDC state (**Supplementary Fig. 8B**). Importantly, we identified TNF-
262 superfamily interactions, including *TNFSF4–TNFRSF4* (OX40L–OX40), *TNFSF9–TNFRSF9* (4-
263 1BBL–4-1BB), *CD70–CD27*, and *PVR*-mediated interactions between mRegDC_2s and CD8$^+$ T_{EX}
264 cells, that were enriched following anti-PD-L1 treatment. These TNF-superfamily molecules promote
265 T cell survival, proliferation, and activation[39]. Moreover, PVR engages activating receptor CD226 or
266 its competing inhibitory receptor TIGIT to control CD8$^+$ T cell effector function[40]. Using IF
267 microscopy, we observed frequent interactions between tumour-residing mRegDCs and Kaede-
268 red$^+$CD3$^+$CD8$^+$ T cells within a perivascular niche, including proliferating (Ki-67$^+$)4-1BB$^+$ cytotoxic
269 cells (**Fig. 5G**, **Supplementary Fig. 8C-F**), consistent with a role for mRegDCs in regulating anti-
270 tumour cytolytic activity.

271 **Conserved mRegDC heterogeneity and CD8$^+$ T cell crosstalk in human cancers**

272 We next asked if the time, tissue, and treatment-associated heterogeneity in mRegDCs observed in our
273 murine model was pertinent to human cancers. In mRegDCs from human CRC (**Supplementary Fig.
274 1B**), there was a gradient of MHC-II expression (**Fig. 6A**). Importantly, markers upregulated on
275 tumour-residing MHC-II^{low} mRegDCs in murine tumours were also preferentially expressed in the
276 human MHC-II^{low} mRegDCs, including *IL15*, *PVR*, *TNFSF4*, *TNFSF9*, and *CD70*.

277 To assess tissue-associated differences in mRegDCs, we analysed an independent human CRC dataset
278 with paired scRNA-seq of tumour, dLN and normal adjacent tissue (**Supplementary Fig. 9A-C**)[45].
279 Consistent with our findings, there was no difference in *CCR7* expression, but *CD80*, *CD86*, *TNFSF4*,
280 *TNFSF9*, *CD70* and *PVR* were higher in tumour-residing mRegDCs versus dLN and normal tissue,
281 while *ICOSLG* was enriched in the dLN (**Fig. 6B**, **Supplementary Fig. 9D-E**). Therefore, the
282 heterogeneity of mRegDCs in murine tumours are paralleled in human CRC.

283 Next, we sought to address whether intra-tumour mRegDCs, and their precise phenotype, influences
284 clinical response to ICB. Atezolizumab (anti-PD-L1 antibody) is widely used in the treatment of
285 metastatic urothelial carcinoma (mUC), but its efficacy is variable[46]. We analysed 208 bulk
286 transcriptomes of tumour biopsies from the IMvigor210 trial for mUC[47,48]. In both responders and non-
287 responders, mRegDC gene expression was positively correlated with effector CD8$^+$ T cell transcripts,
288 and was higher in responders (**Supplementary Fig. 9F**). To leverage the clinical response data from
289 this cohort, we integrated the bulk transcriptomes with scRNA-seq of myeloid cells in mUC[49] (**Fig.
290 6C**) using *Scissor*[50], which enables identification of clinically relevant cell subpopulations and gene
291 expression profiles. This analysis revealed that mRegDCs were enriched in responders (**Fig. 6D**).
292 Indeed, myeloid cells associated with a favourable clinical response expressed transcripts associated
293 with tumour-residing mRegDCs, including *CCR7*, *CD274*, *IL15*, *PVR* and *CD70* (**Fig. 6E**).

294 Moreover, in breast cancer (**Supplementary Fig. 1D**, **9G**)[25], mRegDCs from tumours that successfully
295 underwent T cell clonotype expansion following treatment with anti-PD-1 antibodies were enriched in
296 transcripts associated with our ICB-induced mRegDC_2 cluster, versus non-responders (**Fig. 6F**).
297 mRegDCs from T cell clonotype expanders also upregulated genes contributing to '*interferon gamma
298 response*', '*FcγR-mediated phagocytosis*', '*lymphocyte co-stimulation*', etc. (**Supplementary Fig.**

299 **9H**). Altogether, data from these treatment cohorts support the importance of an ICB-activated
300 mRegDC state.

301 Next, we asked if the molecular crosstalk between mRegDCs and $CD8^+$ T cells in mice is conserved
302 in humans. In PIC-seq data from NSCLC[37], we found that doublets containing mRegDCs highly
303 expressed ligands we had identified in mice (**Fig. 5F**), and their corresponding T cell receptors were
304 highly expressed in the same mRegDC-T cell conjugates (**Fig. 6G**). Moreover, mRegDC-$CD8^+$ T cell
305 doublets were most enriched for T cell cytotoxicity genes and '*TNFα response via NFκB*' compared to
306 other myeloid-$CD8^+$ T cell combinations (**Fig. 6H**, **Supplementary Fig. 9I-J**).

307 Finally, we re-examined hotspots of mRegDC and effector $CD8^+$ T cell co-localisation in spatial
308 transcriptomics of CRC, breast cancer and melanoma (**Fig. 4E**, **Supplementary Fig. 5G-H**).
309 Molecules involved in mRegDC-$CD8^+$ T cell crosstalk were expressed in these voxels, with spatial
310 correlation of mRegDC-$CD8^+$ T cell ligand-receptor pairs in all 3 tumour types (**Fig. 6I-J**,
311 **Supplementary Fig. 10A-C**). Altogether, these data show that mRegDCs are critically positioned to
312 modulate anti-tumour cytolytic activity, including via TNF-superfamily ligands and PVR.

313

314 **Discussion**

315 In this study, we combined scRNA-seq with a photoconvertible murine tumour model to unravel the
316 spatio-temporal dynamics of tumour mRegDCs. Contrary to current assumptions, mRegDCs are
317 heterogeneous, including sub-populations that either primarily contribute to LN migration or are
318 retained in the tumour. We found that mRegDCs acquire transcriptional features consistent with
319 functional "exhaustion" with increasing tumour dwell-time, but following anti-PD-L1 treatment,
320 become skewed towards a state enriched in T cell stimulatory molecules. This heterogeneity, crosstalk
321 with cytotoxic T cells, and association with response to ICB was conserved across human cancers.

322 Our work suggests that mRegDCs serve as a critical immune hub within the TME, through the
323 provision of chemotactic, survival, activating, and regulatory factors. We identified an mRegDC-CD8$^+$
324 T_{EX} cell axis, including specific interactions which may control anti-tumour cytolytic activity.
325 Consistent with this, a recent study showed that acquisition of the full effector CD8$^+$ T cell program
326 requires engagement of CD80^{high} DCs in the local TME[51], which we show are likely mRegDCs. The
327 success of ICB have led to combination immune checkpoint therapy[52], exemplified by the recent
328 success of tiragolumab (anti-TIGIT) + atezolizumab for NSCLC[53]. In CD8$^+$ T cells, mechanistic
329 convergence of PD-1 and TIGIT inhibitory pathways powerfully regulates cytotoxic function[54]. We
330 found that mRegDCs are the major suppliers of both PD-1 and TIGIT ligands to CD8$^+$ T cells, and
331 importantly, there was an increase in PVR expression following anti-PD-L1 treatment, potentially
332 regulating T cell activation via CD226/TIGIT engagement[40]. Independently, combining OX40 agonists
333 with anti-PD-L1 antibodies effectively treated breast cancer in mice[55]. Our data suggest that mRegDCs
334 may contribute to the synergistic mechanisms of novel combinatorial immunotherapies.

335 Several questions remain; While provision of PD-1 ligands by DCs are essential for effective ICB[14,16],
336 it remains unclear whether anti-PD-L1 antibodies directly alter DC function. Interestingly, 'reverse
337 signalling' through PD-L1 has been described[56,57], including effects on DC migration[58]. Moreover,
338 knowledge of mRegDC ontogeny remain incomplete[6,17], including the relative contribution of cDC
339 subsets or monocytes to heterogeneous mRegDC states. Finally, whether the retention of mRegDCs in
340 tumours is due to the acquisition of aberrant trafficking behaviour or due to intratumoral interactions,
341 such as chemoattraction to stromal cells or tumour cells expressing CCR7 ligands [59,60] remains to be
342 resolved. However, recent studies have reported that mRegDCs engage CXCL13$^+$ CD4$^+$ T cells and
343 regulatory T cells in tumours[37,61,62], and may reside in tertiary lymphoid structures[10,13].

344 Previous studies have drawn conflicting conclusions on the role of mRegDCs in tumours; Loss of TIM-
345 3 in DCs prevents the acquisition of the mRegDC programme, but facilitates maintenance of the
346 effector CD8$^+$ T cell pool[63]. Conversely, CXCL16 and IL-15 expressing CCR7$^+$ DCs may recruit and
347 sustain CXCR6$^+$ cytotoxic T cells crucial in cancer immunosurveillance[44]. Our data help to resolve
348 these contradictions; We propose that tumour mRegDCs are heterogeneous, with subset-specific
349 capacity to both support and inhibit the cytotoxic T cell niche, presenting new opportunities for
350 intervention.

351 **Methods**

352 **Mice**

353 Transgenic C57BL/6 Kaede and BALB/c Kaede mice are maintained and bred at the University of
354 Birmingham Biomedical Services Unit. C57BL/6 mice were maintained and bred at the University of
355 Birmingham Biomedical Services Unit or the University of Cambridge Biomedical Services Gurdon
356 Institute animal facilities. Mice were culled between the ages of 8 and 14 weeks. All animal
357 experiments were conducted in accordance with Home Office guidelines and were approved by the
358 University of Birmingham Animal Welfare and Ethical Review Body or the University of Cambridge
359 Animal Welfare and Ethics Review Board. Mice were housed at 21°C, 55% humidity, with 12 h light-
360 dark cycles in 7-7 individually ventilated caging with environmental enrichment of plastic houses plus
361 paper bedding.

362 **Mouse subcutaneous tumour model**

363 MC38 (kindly provided by Dr. Gregory Sonnenberg; Weill Cornell Medicine, New York, NY), CT26
364 (kindly provided by Professor Tim Elliot, University of Oxford, Oxford, UK) and MC38-Ova (obtained
365 from AstraZeneca) murine colon adenocarcinoma cells were cultured in RPMI in supplemented with
366 2mM L-glutamine (Thermo Fisher Scientific), 10% FBS (F9665; Sigma-Aldrich), and penicillin-
367 streptomycin (Sigma-Aldrich) at 37°C with 5% CO2. Cells grown in the log-phase were harvested and
368 resuspended to 2.5×10^6 cells/ml in Dulbecco's PBS (Sigma-Aldrich) for tumour injection.

369 2.5×10^5 tumour cells in 100 µl were subcutaneously injected into mice in the pre-shaved left flank
370 area under anaesthesia via 2% gaseous isoflurane. MC38-Ova tumours were used for scRNA-seq and
371 flow cytometry experiments. MC38 tumours were used for microscopy. CT26 tumours were used for
372 flow cytometry and microscopy. Tumour size was periodically measured with a digital Vernier calliper,
373 and the volume was calculated using the formula $V = 0.5 \times a \times b^2$ in cubic millimetres, where a and b
374 are the long and short diameters of the tumour respectively. Tumour weights were measured at the
375 endpoint of the experiment. Mice were sacrificed on day 14, 15, or 16 (24h, 48h, 72h post-
376 photoconversion respectively, where performed) and tumours were harvested for analysis. Where
377 indicated for specific experiments, tumour-dLNs (i.e. left inguinal LN) and contralateral non-draining
378 lymph nodes were also harvested.

379 **Administration of anti-PD-L1 antibodies**

380 Anti-PD-L1 mouse IgG1 (Clone 80, SP16-260; AstraZeneca) or NIP228 isotype control mouse IgG1
381 (SP16-017; Astra Zeneca) were administered on day 7, 10, and 13 after tumour injection by
382 intraperitoneal injection. Each dose consisted of 200 µg antibodies diluted in 200 µl PBS (10 mg/kg
383 body weight). Tumour volume was measured on day 7, 10, 13 and the experiment endpoint.

384 **Labelling of tumour compartment by photoconversion**

385 Photoconversion was performed as previously described[20,29]. Briefly, on day 13 after tumour injection,
386 the subcutaneous tumour was exposed to a 405-nm wavelength focussed LED light (Dymax BlueWave
387 QX4 outfitted with 8mm focussing length, DYM41572; Intertronics) for 3 minutes, with a 5-second
388 break every 20 seconds, at a fixed distance of 1 cm. Black cardboard was used to shield the remainder
389 of the mouse. We previously showed that this method resulted in complete conversion (99.9%) of host
390 cells within the tumour from the default green fluorescence of the Kaede protein (Kaede-green) to the
391 altered red fluorescence (Kaede-red), and that the cells in the dLN were fully protected from tumour
392 photoconversion[20]. Of note, while converted cells express Kaede-red fluorescence, they also retain a

weak Kaede-green signal. Overall, this enabled the discrimination of newly infiltrating (Kaede-green) and resident (Kaede-red) cell populations in the tumour, or cells that have egressed the tumour (Kaede-red) by their fluorescence profile. Moreover, using i.v. administration of anti-CD45 antibodies prior to culling, we previously showed that majority of cells (>95%) were in tumour tissue and were not intravascular contaminants[20].

Confocal microscopy

Tumour or LN samples were fixed in 1% paraformaldehyde (Electron Microscopy Services) for 24h at 4°C followed by 12h in 30% sucrose in PBS. 20µm sections were permeabilized and blocked in 0.1M TRIS, containing 0.1% Triton (Sigma), 1% normal mouse serum, 1% normal rat serum and 1% BSA (R&D Systems). Samples were stained for 2h at RT in a humid chamber with the appropriate antibodies, listed in Supplementary table 1, washed 3 times in PBS and mounted in Fluoromount-G® (Southern Biotech). Images were acquired using a TCS SP8 (Leica microsystems, Milton Keynes, UK) confocal microscope. Raw imaging data were processed using Imaris v9.7.2 (Bitplane).

Iterative staining of sections was performed as previously described[64]. Samples were prepared and stained as detailed above. Following acquisition, the coverslips were removed, and slides were washed 3 times in PBS to remove residual mounting medium. Bleaching of the fluorochromes were achieved by submerging the slide in a 1mg/mL solution of lithium borohydride in water (Acros Organics) for 15 minutes at room temperature. The slides were then washed 3 times in PBS prior to staining with a different set of antibodies. The process was repeated twice. Raw imaging data were processed using Imaris using CD31 as fiducial for the alignment of acquired images.

Tissue dissociation

Tumours were cut into small pieces using surgical scissors, and incubated with 1 mg/ml collagenase D (Roche) and 0.1 mg/ml DNase I (Roche) in a volume of 1.2 ml RPMI media at 37°C on a thermomixer (Eppendorf) for 20 min; or tumours were digested using Tumour Dissociation Kit (Miltenyi Biotec) and gentleMACS Dissociator (Miltenyi Biotec) for 40 minutes at 37°C according to the manufacturer's protocol. The gentleMACS protocol was used for scRNA-seq experiments. Subsequently, the sample was filtered through a 70 µm strainer to remove undigested tissue debris. Next, dead cells were removed using Dead Cell Removal Kit and LS Columns (Miltenyi Biotec), according to the manufacturer's instructions. Lymph nodes were cleaned and dissected in RPMI 1640 medium (Thermo Fisher Scientific) and crushed through a 70 µm strainer. Thereafter, cells were centrifuged at 400 *g* at 4°C for 5 min and resuspended in FACS staining buffer (2% FBS; 2mM EDTA in PBS) for flow cytometry.

Flow cytometry

Cell suspensions were subjected to Fc block with anti-CD16/32 (BioLegend) diluted in FACS staining buffer on ice for 15 min before staining with a Live/Dead stain and surface markers, listed in Supplementary table 1, diluted in FACS staining buffer on ice for 30 min. Where applicable, cells were then fixed with Cytofix fixation buffer (BD) for 45 min and stained for intracellular markers diluted in eBioscience permeabilization buffer (Thermo Fisher) at room temperature overnight. 1 x 10^4 counting beads (Spherotech) were added to stained samples at the final step, to calculate absolute cell numbers. Data were acquired on the LSR Fortessa X-20 (BD) using FACSDiva v8.0.2 software (BD) or CytoFLEX (Beckman Coulter) using CytExpert v2.5 (Beckman Coulter) and analysed with FlowJo v10.8.1 (BD).

435 **Single-cell isolation**

436 MC38-Ova tumours were injected in age-matched female C57BL/6 mice, treated with anti-PD-L1
437 antibodies, and photoconverted on day 13 as described above. Mice with tumours of similar sizes were
438 collected 48h after tumour photoconversion. After tumour digestion, as described above, cell
439 suspensions were stained for CD45 BV786, TER119 PE-Cy7, CD11b BV421, NK1.1 BV650,
440 Live/dead APC-Cy7 on ice for 30 min (Supplementary table 1). Subsequently, cells were centrifuged
441 at 400 *g* at 4°C for 5 min and resuspended in FACS staining buffer for sorting. Tumour-infiltrating
442 lymphocytes (Live $CD45^{+}TER119^{-}Kaede^{+}CD11b^{-/lo}NK1.1^{lo/hi}$) and tumour-infiltrating myeloid cells
443 (Live $CD45^{+}TER119^{-}Kaede^{+}CD11b^{+}NK1.1^{-}$) from anti-PD-L1 or isotype-control treated tumours
444 were sorted with a FACS Aria II Cell Sorter (BD) into two groups per condition, based on the presence
445 or absence of Kaede-red signal.

446 Tumour-dLNs from mice treated with the same experimental protocol were harvested and digested as
447 described in the preceding paragraph. Cell suspensions were stained for CD45 BV785, TER119 PE-
448 Cy7, Live/dead APC-Cy7 on ice for 30 min. Live $CD45^{+}Ter119^{-}Kaede^{+}Kaede\text{-}red^{+}$ cells were sorted,
449 to identify immune cells that have migrated from photoconverted tumours (Kaede-red) to the tumour-
450 dLNs. Inguinal lymph nodes from control mice (no tumour cells injected) were also processed for
451 scRNA-seq to obtain a representation of homeostatic cell populations in the LN. This was done to
452 facilitate accurate annotation and integration of Kaede-red cells in the tumour-dLN, where specific
453 populations arriving from the tumour would be disproportionately over-represented, with the LN
454 cellular landscape. Control LN cell suspensions were stained for B220 BV421, CD11c BV786,
455 TER119 PE-Cy7, Live/dead APC-Cy7 on ice for 30 min. Thereafter, a 3-way sort was performed
456 consisting of Live $Kaede^{+}TER119^{-}CD11c^{+}B220^{-}$ (myeloid), $Kaede^{+}TER119^{-}CD11c^{-}B220^{+}$ (B cells),
457 and $Kaede^{+}TER119^{-}CD11c^{-}B220^{-}$ fractions. The three subsets were then mixed at a ratio of 1:1:1 to
458 generate a cellular suspension enriched for DCs and with reduced frequency of B cells. scRNA-seq of
459 control LNs and tumour-dLNs were sequenced and analysed together.

460 **Single-cell library construction and sequencing**

461 Gene expression libraries from were prepared from FACS-sorted populations of single cells using the
462 Chromium Controller and Chromium Single Cell 3' GEM Reagent Kits v3 (10x genomics, Inc.)
463 according to the manufacturer's protocol. The resulting sequencing libraries comprised of standard
464 Illumina paired-end constructs flanked with P5 and P7 sequences. The 16 bp 10x barcode and 10 bp
465 UMI were encoded in read 1, while read 2 was used to sequence the cDNA fragment. Sample index
466 sequences were incorporated as the i7 index read. Paired-end sequencing (2 x 150 bp) was performed
467 on the Illumina NovaSeq 6000 platform. The resulting .bcl sequence data were processed for QC
468 purposes using bcl2fastq software (v2.20.0.422) and the resulting fastq files were assessed using
469 FastQC (v0.11.3), FastqScreen (v0.9.2) and FastqStrand (v0.0.5) prior to alignment and processing
470 with the CellRanger (v6.1.2) pipeline.

471 **Processing of scRNA-seq**

472 Single-cell gene expression data from CellRanger count output (filtered features, barcodes, and
473 matrices) were analysed using the Scanpy[65] (v1.8.2) workflow. Raw count data from the myeloid and
474 TIL sorts were concatenated. Doublet detection was performed using Scrublet[66] (v0.2.1), with cells
475 from iterative sub-clustering flagged with outlier Scrublet scores labelled as potential doublets. Cells
476 with counts mapped to >6000 or <1000 genes were filtered. The percentage mitochondrial content cut-
477 off was set at <7.5%. Genes detected in fewer than 3 cells were filtered. Total gene counts for each cell
478 were normalised to a target sum of 10^4 and log1p transformed. There resulted in a working dataset of

479 80,556 cells. Next, highly variable features were selected based on a minimum and maximum mean
480 expression of ≥0.0125 and ≤3 respectively, with a minimum dispersion of 0.5. Total feature counts,
481 mitochondrial percentage, and cell cycle scores, where indicated, were regressed out. The number of
482 principal components used for neighbourhood graph construction was set to 50 initially, and
483 subsequently 30 for myeloid and TIL subgroup processing. Clustering was performed using the Leiden
484 algorithm with resolution set at 1.5 for initial annotations, but subsequently sub-clustering was
485 performed at lower resolutions (0.7-1.0) for analysis of myeloid cell, DC, T cell, and $CD8^+$ T cell
486 subsets. Uniform manifold approximation and projection (UMAP, v0.5.1) was used for dimensional
487 reduction and visualisation, with a minimum distance of 0.3, and all other parameters according to the
488 default settings in Scanpy.

489 **Analysis of scRNA-seq from mouse tumour models**

490 Broad cell types of interest were subset (eg. DCs from myeloid cells) and re-clustered as described
491 above. Resulting clusters were annotated using canonical marker gene expression and published
492 transcriptomic signatures. Unless otherwise indicated, log-transformed expression values were used
493 for plotting. Gene set scoring was performed using Scanpy's tl.score_genes tool. Gene sets were
494 obtained from the Molecular Signature Database (MSigDB) inventory, specifically Hallmark, KEGG,
495 or Gene Ontology (GO), using the R package msigdbr (v7.5.1) or published RNAseq data
496 (Supplementary table 2). The original published mRegDC signature gene list[5] was used for the initial
497 scoring and identification of mRegDCs. Differential gene testing was performed using the Wilcoxon
498 rank sum test implemented in Scanpy's tl.rank_genes_groups. Analysis of MC38-Ova and B16
499 tumours and their dLNs followed these same methods.

500 Trajectory analysis was performed using partition-based graph abstraction (PAGA)[67] and the Palantir
501 algorithm[68]. For Palantir pseudo-time analysis, the differentiation trajectory was rooted in the Kaede-
502 green dominant cluster, which represents the cellular subset most associated with newly-infiltrating
503 cells. Integration and label transfer of lymph node DC scRNA-seq data and tumour DCs, or cycling
504 $CD8^+$ T cells and non-cycling $CD8^+$ T cells was performed using Scanpy's tl.ingest tool. For analysis
505 of cycling $CD8^+$ T cells, cell cycle regression was first performed on the isolated cluster using Scanpy's
506 pp.regress_out function, before re-integration.

507 Gaussian kernel density estimation to compute density of cells in the UMAP embedding was performed
508 using Scanpy's tl.embedding_density. Differential abundance analysis was performed using Milo.
509 Spcifically, the *k*-nearest-neighbour (kNN) graph was constructed with a *k* parameter of 30 and initial
510 random sampling rate of 0.1. Cellular neighbourhoods with constituent cells comprising less than 70%
511 of a previously defined cluster were designated as mixed neighbourhoods. CellPhoneDB[43] (v2.1.7) was
512 used for cell-cell communication analysis, using the default parameters and normalised expression
513 values as the input. CellPhoneDB output was visualised using ktplots
514 (https://github.com/zktuong/ktplots).

515 For pathway analysis between Kaede-red versus Kaede-green or anti-PD-L1 versus isotype control
516 groups in the scRNA-seq dataset, a pseudo-bulk approach was first applied to single-cell gene
517 expression data (https://github.com/colin-leeyc/CLpseudobulk), to increase robustness for pathway
518 analysis and overcome limitations associated with differential expression testing on single cells[69].
519 Briefly, filtered, raw count data (prior to normalisation, transformation, or scaling) from each condition
520 were randomly sorted into artificial replicates, with iterative bootstrapping applied to random sampling
521 (n >10). Pseudo-bulked count matrices were normalised using the median-of-ratios method,
522 implemented in DESeq2[70] (v1.34), and differential gene expression testing was performed using the
523 Wald test. Pre-ranked gene set enrichment analysis[71] (GSEA) was implemented in fgsea (v1.24), using

524 the averaged Wald statistic over n >10 iterations of random sorting into pseudo-bulked replicates, as
525 the gene rank metric. Leading edge genes were identified for further analysis. GO term over-
526 representation analysis was implemented in topGO[72] (v2.50), using the top 100 genes with the highest
527 loadings for each principal component (PC) of interest, following PC analysis.

528 **Analysis of scRNA-seq from human tumours**

529 scRNA-seq data from human solid tumours were downloaded from public repositories, which are listed
530 under *Data availability* with references. Where necessary, data access permissions were sought and
531 approved prior to download. Data was analysed using the Scanpy (v1.8.2) workflow, as outlined in the
532 sections above. Filtering for quality control was performed according to the parameters outlined in the
533 original publications. scRNA-seq integration was performed using the batch-balanced KNN (with
534 ridge regression) approach or Harmony algorithm with sequencing batch as the batch term, where
535 available and sufficient, or patient ID if sequencing batch was not available. Cell annotations from
536 original publications were checked and refined, particularly where myeloid cell annotations were not
537 complete or the focus of the original publication.

538 Myeloid cells were subset and used for further analysis. In total, this included re-analysis of 41,624
539 and 43,193 myeloid cells from two independent CRC datasets, 16,688 myeloid cells from breast
540 tumours, 8,555 myeloid cells from cutaneous melanoma, 11,663 myeloid or T cells from NSCLC
541 including 901 myeloid-T cell doublets, and 1,988 myeloid cells from metastatic urothelial carcinoma.
542 mRegDCs were identified using expression of migratory transcripts and mRegDC signature genes[5].

543 The only exception to the Scanpy workflow was for analysis of NSCLC PICseq data, where the
544 Metacell workflow was utilised, as documented in the original publication, for analysis and annotation
545 of single-cells[37]. This was to ensure compatibility with the PICseq deconvolution algorithm[73], which
546 was used to analyse sorted doublets. Gene expression raw count data from PICs only were obtained
547 and input to the Scanpy workflow for visualisation and further analysis. Doublet deconvolution results
548 for contributing myeloid cell or T cell identities in each PIC were retained.

549 Subsequently, analysis of gene expression profiles, gene signature scoring, cell-cell communication,
550 were as described in earlier sections. For analysis of enrichment of mRegDC_2 genes in the breast
551 cancer dataset, where anti-PD-1 response data was available, mRegDC_2 genes were first identified
552 as DEGs between mRegDC_2 versus remaining mRegDCs (Wilcoxon rank-sum test) in scRNA-seq
553 from murine tumours. 85 differentially upregulated genes (p-adj < 0.05, $\log_2$Fold-change > 1) were
554 converted to equivalent human gene symbols using Ensembl and used to score mRegDCs from human
555 breast cancer (Fig. 6F).

556 **Analysis of bulk transcriptomics**

557 Bulk RNA-seq data were downloaded from public repositories, listed under *Data availability* with
558 references. Where necessary, data access permissions were sought and approved prior to download.
559 TCGA data was accessed via TCGAbiolinks, using STAR-aligned reads[24]. For bulk transcriptomics
560 data from both TCGA and the IMvigor 210 trial, transcripts-per-million (tpm) normalised values were
561 used for analysis. Cellular deconvolution was performed using xCell[74], implemented in the webtool
562 using default parameters. Gene signatures scoring was performed using single-sample GSEA[75]
563 (ssGSEA, v10.1.0), implemented in GenePattern, followed by normalisation (scaled between 0 and 1)
564 of gene set enrichment scores. Cell type signatures for ssGSEA were derived from cell-specific
565 differentially expressed genes in scRNA-seq of human cancers. Pearson correlation was used to assess
566 for correlation of cellular proportions or cell-specific signatures of interests in biopsy samples. Survival

analysis was performed on overall survival (months), using the median mRegDC signature score for stratification to 'high' and 'low' groups, and log-rank test was applied to survival curves. For integration of bulk transcriptomic data from the IMvigor210 trial with accompanying clinical response data with scRNA-seq of myeloid cells in mUC, the Scissor pipeline was used[50]. Scissor enables identification of single-cells and gene expression profiles within cell subpopulations that are significantly associated with phenotypes obtained from bulk expression data. A logistic regression model using the binary outcome of clinical responders (CR/PR) vs non-responders (SD/PD) was used, and the alpha parameter was set at 0.05, per default settings.

Raw RNA-seq sequencing data from PD-L1 knockout (KO) mice injected with wild-type (WT) MC38 tumour cells, WT mice injected with PD-L1 KO tumours, PD-L1 KO mice injected with PD-L1 KO tumours, and WT mice injected with WT tumours was aligned and quantified using Salmon and tximport[15]. Analysis was performed using the standard DESeq2 workflow and GSEA was used for pathway analysis.

Analysis of spatial transcriptomics

10x Visium spatial transcriptomics were analysed using the standard Scanpy (v1.8.2) workflow, using the default SpaceRanger outputs including spot alignments to corresponding tissue haematoxylin and eosin or immune-fluorescence images. Spots with fewer <500 counts, >80000 counts, and percentage mitochondrial content >15% were filtered. Genes detected in fewer than 5 spots were filtered. Total feature counts, mitochondrial percentage, and cell cycle scores were regressed out. Expression values plotted are log1p-transformed 10^4-sum-normalised values. Gene set scoring was performed using Scanpy's tl.score_genes tool. Calculation of spatial correlation was implemented using the correlationSpot function in ktplots (https://github.com/zktuong/ktplots), as previously described[76]. Briefly, k = 6 nearest neighbourhoods were extracted from a kNN graph computed from the spatial location of each Visium spot. Pearson correlation was performed on each neighbourhood using gene expression values or gene signature scores and averaged across the neighbourhoods. Correlation values were only returned if expression value or signature scores were detected in all spots. Spots with positive correlation scores were plotted, which represent areas of co-localisation.

Statistical analysis

Mice were gender-matched (all female). Tumour growth curves for anti-PD-L1 and isotype control treated groups were analysed using two-way ANOVA and Sidak's multiple comparisons test and are presented as mean ± SEM. Analysis for RNA sequencing is as described above, including statistical frameworks used. Statistical tests were implemented for two principal purposes; to compare expression values (RNA or protein) between samples, or to compare proportions of defined cell subsets. All experiments were performed with biological replicates, and the specific statistical tests applied are indicated in the figure legends. All statistical tests applied were two-tailed. Paired statistical tests were used where different populations from the same animal were compared. All animal experiments were randomised prior to experimental intervention. Statistical significance are denoted as follows: ns, not significant; $*P < 0.05$; $**P < 0.01$; $***P < 0.001$; $****P < 0.0001$. Statistical analyses were performed in R or GraphPad Prism.

Online supplemental material

Supplementary table 1 list antibodies used. Supplementary table 2 list gene sets used.

Data and code availability

609 The scRNA-seq data have been deposited on the GEO public repository under accension numbers
610 GSExxxxxxx and GSExxxxxx (*available upon manuscript publication*). Additional data or
611 information will be made available upon reasonable request. Published data was accessed and
612 downloaded from public GEO, SRA, EGA and Synapse repositories using the following ascension
613 numbers: scRNA-seq of CRC (GSE178341 and syn26844071)[27,45]; scRNA-seq of breast cancer
614 (EGAS00001004809)[25]; scRNA-seq of melanoma (GSE123139)[26]; scRNA-seq of mUC
615 (HRA000212)[49]; scRNA-seq and PICseq of NSCLC (GSE160903)[37]; TCGA
616 (https://portal.gdc.cancer.gov, via TCGAbiolinks)[24]; IMvigor210 bulk RNA-seq
617 (EGAS00001004343)[47]; 10x Visium (https://www.10xgenomics.com/resources/datasets)[36]; PD-L1
618 knockout bulk RNA-seq (PRJNA356678)[15]. All analysis performed are described in detail under
619 *Methods*. Source code for key softwares or computational pipelines used have been cited. Additional
620 code used for analysis, as described above, have been made available on GitHub repositories.

621

622 **References**

623 1. Wculek, S. K. *et al.* Dendritic cells in cancer immunology and immunotherapy. *Nature Reviews*
624 *Immunology 2019 20:1* **20**, 7–24 (2019).
625 2. Roberts, E. W. *et al.* Critical Role for CD103(+)/CD141(+) Dendritic Cells Bearing CCR7 for Tumor
626 Antigen Trafficking and Priming of T Cell Immunity in Melanoma. *Cancer Cell* **30**, 324–336 (2016).
627 3. Sallusto, F. *et al.* Rapid and coordinated switch in chemokine receptor expression during dendritic cell
628 maturation. *Eur J Immunol* **28**, 2760–2769 (1998).
629 4. Böttcher, J. P. & Reis e Sousa, C. The Role of Type 1 Conventional Dendritic Cells in Cancer Immunity.
630 *Trends Cancer* **4**, 784–792 (2018).
631 5. Maier, B. *et al.* A conserved dendritic-cell regulatory program limits antitumour immunity. *Nature* **580**,
632 257–262 (2020).
633 6. Kvedaraite, E. & Ginhoux, F. Human dendritic cells in cancer. *Sci Immunol* **7**, (2022).
634 7. Gerhard, G. M., Bill, R., Messemaker, M., Klein, A. M. & Pittet, M. J. Tumor-infiltrating dendritic cell
635 states are conserved across solid human cancers. *Journal of Experimental Medicine* **218**, (2021).
636 8. Cheng, S. *et al.* A pan-cancer single-cell transcriptional atlas of tumor infiltrating myeloid cells. *Cell*
637 **184**, 792-809.e23 (2021).
638 9. Zilionis, R. *et al.* Single-Cell Transcriptomics of Human and Mouse Lung Cancers Reveals Conserved
639 Myeloid Populations across Individuals and Species. *Immunity* **50**, 1317-1334.e10 (2019).
640 10. Goc, J. *et al.* Dendritic cells in tumor-associated tertiary lymphoid structures signal a th1 cytotoxic
641 immune contexture and license the positive prognostic value of infiltrating CD8+ t cells. *Cancer Res* **74**,
642 705–715 (2014).
643 11. Movassagh, M. *et al.* Selective Accumulation of Mature DC-Lamp+ Dendritic Cells in Tumor Sites Is
644 Associated with Efficient T-Cell-Mediated Antitumor Response and Control of Metastatic
645 Dissemination in Melanoma. *Cancer Res* **64**, 2192–2198 (2004).
646 12. de Mingo Pulido, Á. *et al.* TIM-3 Regulates CD103+ Dendritic Cell Function and Response to
647 Chemotherapy in Breast Cancer. *Cancer Cell* **33**, 60-74.e6 (2018).
648 13. Dieu-Nosjean, M. C. *et al.* Long-term survival for patients with non-small-cell lung cancer with
649 intratumoral lymphoid structures. *J Clin Oncol* **26**, 4410–4417 (2008).
650 14. Peng, Q. *et al.* PD-L1 on dendritic cells attenuates T cell activation and regulates response to immune
651 checkpoint blockade. *Nature Communications 2020 11:1* **11**, 1–8 (2020).
652 15. Lau, J. *et al.* Tumour and host cell PD-L1 is required to mediate suppression of anti-tumour immunity in
653 mice. *Nature Communications 2017 8:1* **8**, 1–11 (2017).
654 16. Oh, S. A. *et al.* PD-L1 expression by dendritic cells is a key regulator of T-cell immunity in cancer.
655 *Nature Cancer 2020 1:7* **1**, 681–691 (2020).
656 17. Ginhoux, F., Guilliams, M. & Merad, M. Expanding dendritic cell nomenclature in the single-cell era.
657 *Nature Reviews Immunology 2022 22:2* **22**, 67–68 (2022).
658 18. Zhang, Q. *et al.* Landscape and Dynamics of Single Immune Cells in Hepatocellular Carcinoma. *Cell*
659 **179**, 829-845.e20 (2019).
660 19. Germain, C. *et al.* Presence of B cells in tertiary lymphoid structures is associated with a protective
661 immunity in patients with lung cancer. *Am J Respir Crit Care Med* **189**, 832–844 (2014).
662 20. Li, Z. *et al.* In vivo labeling reveals continuous trafficking of TCF-1+ T cells between tumor and
663 lymphoid tissue. *J Exp Med* **219**, (2022).
664 21. Wherry, E. J. T cell exhaustion. *Nat Immunol* **12**, 492–499 (2011).
665 22. Gao, Y. *et al.* Tumor immunoevasion by the conversion of effector NK cells into type 1 innate lymphoid
666 cells. *Nat Immunol* **18**, 1004–1015 (2017).
667 23. Platonova, S. *et al.* Profound coordinated alterations of intratumoral NK cell phenotype and function in
668 lung carcinoma. *Cancer Res* **71**, 5412–5422 (2011).

669 24. The Cancer Genoma Atlas. TCGA. *National Cancer Institute (NCI) and National Human Genome*
670 *Research Institute (NHGRI)* (2013).
671 25. Bassez, A. *et al.* A single-cell map of intratumoral changes during anti-PD1 treatment of patients with
672 breast cancer. *Nat Med* **27**, 820–832 (2021).
673 26. Li, H. *et al.* Dysfunctional CD8 T Cells Form a Proliferative, Dynamically Regulated Compartment
674 within Human Melanoma. *Cell* **176**, 775-789.e18 (2019).
675 27. Pelka, K. *et al.* Spatially organized multicellular immune hubs in human colorectal cancer. *Cell* **184**,
676 4734-4752.e20 (2021).
677 28. Curtis, C. *et al.* The genomic and transcriptomic architecture of 2,000 breast tumours reveals novel
678 subgroups. *Nature* **486**, 346–352 (2012).
679 29. Tomura, M. *et al.* Monitoring cellular movement in vivo with photoconvertible fluorescence protein
680 'Kaede' transgenic mice. *Proc Natl Acad Sci U S A* **105**, 10871–10876 (2008).
681 30. Riley, J. L., Westerheide, S. D., Price, J. A., Brown, J. A. & Boss, J. M. Activation of class II MHC
682 genes requires both the X □ region and the class II transactivator (CIITA). *Immunity* **2**, 533–543 (1995).
683 31. Miller, J. C. *et al.* Deciphering the transcriptional network of the DC lineage. *Nat Immunol* **13**, 888
684 (2012).
685 32. Riley, J. L. *et al.* Modulation of TCR-induced transcriptional profiles by ligation of CD28, ICOS, and
686 CTLA-4 receptors. *Proc Natl Acad Sci U S A* **99**, 11790–11795 (2002).
687 33. Garris, C. S. *et al.* Successful Anti-PD-1 Cancer Immunotherapy Requires T Cell-Dendritic Cell
688 Crosstalk Involving the Cytokines IFN-γ and IL-12. *Immunity* **49**, 1148-1161.e7 (2018).
689 34. Dubois, S. P., Waldmann, T. A. & Müller, J. R. Survival adjustment of mature dendritic cells by IL-15.
690 *Proc Natl Acad Sci U S A* **102**, 8662 (2005).
691 35. Davidson, S. *et al.* Single-Cell RNA Sequencing Reveals a Dynamic Stromal Niche That Supports
692 Tumor Growth. *Cell Rep* **31**, (2020).
693 36. 10x Genomics. 10x Genomics Spatial Gene Expression. *Visium demonstration dataset*
694 https://www.10xgenomics.com/resources/datasets (2022).
695 37. Cohen, M. *et al.* The interaction of CD4+ helper T cells with dendritic cells shapes the tumor
696 microenvironment and immune checkpoint blockade response. *Nat Cancer* **3**, 303–317 (2022).
697 38. Dann, E., Henderson, N. C., Teichmann, S. A., Morgan, M. D. & Marioni, J. C. Differential abundance
698 testing on single-cell data using k-nearest neighbor graphs. *Nat Biotechnol* **40**, 245–253 (2022).
699 39. Croft, M. The role of TNF superfamily members in T-cell function and diseases. *Nature Reviews*
700 *Immunology 2009 9:4* **9**, 271–285 (2009).
701 40. Johnston, R. J. *et al.* The Immunoreceptor TIGIT Regulates Antitumor and Antiviral CD8+ T Cell
702 Effector Function. *Cancer Cell* **26**, 923–937 (2014).
703 41. Im, S. J. *et al.* Defining CD8+ T cells that provide the proliferative burst after PD-1 therapy. *Nature* **537**,
704 417–421 (2016).
705 42. Singer, M. *et al.* A Distinct Gene Module for Dysfunction Uncoupled from Activation in Tumor-
706 Infiltrating T Cells. *Cell* **166**, 1500-1511.e9 (2016).
707 43. Efremova, M., Vento-Tormo, M., Teichmann, S. A. & Vento-Tormo, R. CellPhoneDB: inferring cell–
708 cell communication from combined expression of multi-subunit ligand–receptor complexes. *Nature*
709 *Protocols 2020 15:4* **15**, 1484–1506 (2020).
710 44. di Pilato, M. *et al.* CXCR6 positions cytotoxic T cells to receive critical survival signals in the tumor
711 microenvironment. *Cell* **184**, 4512-4530.e22 (2021).
712 45. Joanito, I. *et al.* Single-cell and bulk transcriptome sequencing identifies two epithelial tumor cell states
713 and refines the consensus molecular classification of colorectal cancer. *Nature Genetics 2022 54:7* **54**,
714 963–975 (2022).

715 46. Rosenberg, J. E. *et al.* Atezolizumab in patients with locally advanced and metastatic urothelial
716 carcinoma who have progressed following treatment with platinum-based chemotherapy: a single-arm,
717 multicentre, phase 2 trial. *Lancet* **387**, 1909–1920 (2016).
718 47. Banchereau, R. *et al.* Molecular determinants of response to PD-L1 blockade across tumor types. *Nature*
719 *Communications 2021 12:1* **12**, 1–11 (2021).
720 48. Balar, A. v. *et al.* Atezolizumab as first-line treatment in cisplatin-ineligible patients with locally
721 advanced and metastatic urothelial carcinoma: a single-arm, multicentre, phase 2 trial. *The Lancet* **389**,
722 67–76 (2017).
723 49. Chen, Z. *et al.* Single-cell RNA sequencing highlights the role of inflammatory cancer-associated
724 fibroblasts in bladder urothelial carcinoma. *Nature Communications 2020 11:1* **11**, 1–12 (2020).
725 50. Sun, D. *et al.* Identifying phenotype-associated subpopulations by integrating bulk and single-cell
726 sequencing data. *Nature Biotechnology 2021 40:4* **40**, 527–538 (2021).
727 51. Prokhnevska, N. *et al.* CD8+ T cell activation in cancer comprises an initial activation phase in lymph
728 nodes followed by effector differentiation within the tumor. *Immunity* **56**, 107-124.e5 (2022).
729 52. Yi, M. *et al.* Combination strategies with PD-1/PD-L1 blockade: current advances and future directions.
730 *Molecular Cancer 2022 21:1* **21**, 1–27 (2022).
731 53. Cho, B. C. *et al.* Tiragolumab plus atezolizumab versus placebo plus atezolizumab as a first-line
732 treatment for PD-L1-selected non-small-cell lung cancer (CITYSCAPE): primary and follow-up
733 analyses of a randomised, double-blind, phase 2 study. *Lancet Oncol* **23**, 781–792 (2022).
734 54. Banta, K. L. *et al.* Mechanistic convergence of the TIGIT and PD-1 inhibitory pathways necessitates co-
735 blockade to optimize anti-tumor CD8+ T cell responses. *Immunity* **55**, 512-526.e9 (2022).
736 55. Lee, J. v. *et al.* Combinatorial immunotherapies overcome MYC-driven immune evasion in triple
737 negative breast cancer. *Nature Communications 2022 13:1* **13**, 1–12 (2022).
738 56. Gato-Cañas, M. *et al.* PDL1 Signals through Conserved Sequence Motifs to Overcome Interferon-
739 Mediated Cytotoxicity. *Cell Rep* **20**, 1818–1829 (2017).
740 57. Clark, C. A. *et al.* Tumor-Intrinsic PD-L1 Signals Regulate Cell Growth, Pathogenesis, and Autophagy
741 in Ovarian Cancer and Melanoma. *Cancer Res* **76**, 6964–6974 (2016).
742 58. Lucas, E. D. *et al.* PD-L1 Reverse Signaling in Dermal Dendritic Cells Promotes Dendritic Cell
743 Migration Required for Skin Immunity. *Cell Rep* **33**, (2020).
744 59. Whyte, C. E. *et al.* ACKR4 restrains antitumor immunity by regulating CCL21. *Journal of Experimental*
745 *Medicine* **217**, (2020).
746 60. Cheng, H. W. *et al.* CCL19-producing fibroblastic stromal cells restrain lung carcinoma growth by
747 promoting local antitumor T-cell responses. *Journal of Allergy and Clinical Immunology* **142**, 1257-
748 1271.e4 (2018).
749 61. Thumkeo, D. *et al.* PGE2-EP2/EP4 signaling elicits immunosuppression by driving the mregDC-Treg
750 axis in inflammatory tumor microenvironment. *Cell Rep* **39**, (2022).
751 62. Magen, A. *et al.* Intratumoral mregDC and CXCL13 T helper niches enable local differentiation of CD8
752 T cells following PD-1 blockade. *bioRxiv* 2022.06.22.497216 (2022) doi:10.1101/2022.06.22.497216.
753 63. Dixon, K. O. *et al.* TIM-3 restrains anti-tumour immunity by regulating inflammasome activation. *Nature*
754 **595**, 101 (2021).
755 64. Radtke, A. J. *et al.* IBEX: A versatile multiplex optical imaging approach for deep phenotyping and
756 spatial analysis of cells in complex tissues. *Proc Natl Acad Sci U S A* **117**, 33455–33465 (2020).
757 65. Wolf, F. A., Angerer, P. & Theis, F. J. SCANPY: Large-scale single-cell gene expression data analysis.
758 *Genome Biol* **19**, 1–5 (2018).
759 66. Wolock, S. L., Lopez, R. & Klein, A. M. Scrublet: Computational Identification of Cell Doublets in
760 Single-Cell Transcriptomic Data. *Cell Syst* **8**, 281-291.e9 (2019).
761 67. Wolf, F. A. *et al.* PAGA: graph abstraction reconciles clustering with trajectory inference through a
762 topology preserving map of single cells. *Genome Biol* **20**, 1–9 (2019).

763 68. Setty, M. *et al.* Characterization of cell fate probabilities in single-cell data with Palantir. *Nat Biotechnol*
764 **37**, 451–460 (2019).
765 69. Squair, J. W. *et al.* Confronting false discoveries in single-cell differential expression. *Nature*
766 *Communications 2021 12:1* **12**, 1–15 (2021).
767 70. Love, M. I., Huber, W. & Anders, S. Moderated estimation of fold change and dispersion for RNA-seq
768 data with DESeq2. *Genome Biol* **15**, (2014).
769 71. Subramanian, A. *et al.* Gene set enrichment analysis: A knowledge-based approach for interpreting
770 genome-wide expression profiles. *Proc Natl Acad Sci U S A* **102**, 15545–15550 (2005).
771 72. Alexa, A. & Rahnenfuhrer, J. topGO: Enrichment Analysis for Gene Ontology. Preprint at (2022).
772 73. Giladi, A. *et al.* Dissecting cellular crosstalk by sequencing physically interacting cells. *Nature*
773 *Biotechnology 2020 38:5* **38**, 629–637 (2020).
774 74. Aran, D., Hu, Z. & Butte, A. J. xCell: Digitally portraying the tissue cellular heterogeneity landscape.
775 *Genome Biol* **18**, 220 (2017).
776 75. Barbie, D. A. *et al.* Systematic RNA interference reveals that oncogenic KRAS-driven cancers require
777 TBK1. *Nature* **462**, 108–112 (2009).
778 76. Tuong, Z. K. *et al.* Resolving the immune landscape of human prostate at a single-cell level in health and
779 cancer. *Cell Rep* **37**, (2021).
780
781

782 **Author Contributions**

783 CYCL processed and analysed sequencing data, designed and performed experiments, analysed data,
784 and wrote the manuscript. BCK, NR, ZL and ID performed experiments and analysed data. ZKT and
785 TH provided project guidance. CW, SW and DP performed experiments. GC, SAH and SJD provided
786 input and reviewed the manuscript. RR supported the project. DW conceived the project, designed
787 experiments, provided guidance, and edited the manuscript. MRC conceived the project, designed
788 experiments, provided guidance, and wrote the manuscript.

789 **Funding**

790 CYCL is funded by the Gates Cambridge scholarship trust and University of Cambridge School of
791 Clinical Medicine Elmore fund. BCK was supported by Cancer Research UK (SEBSTF-2021/100002).
792 ID is supported by an iCASE Studentship with AstraZeneca. DRW is funded by Cancer Research UK
793 Immunology Project Award C54019/A27535, Cancer Research Institute CLIP grant CRI3128,
794 Worldwide Cancer Research Grant 21-0073 and a Medical Research Council IMPACT iCASE
795 Studentship with AstraZeneca. MRC is supported by the National Institute of Health Research (NIHR)
796 Cambridge Biomedical Research Centre and the NIHR Blood and Transplant Research Unit and a
797 Wellcome Investigator Award (220268/Z/20/Z).

798 **Acknowledgments**

799 We thank A. Ptasinska and other members of Genomics Birmingham at University of Birmingham for
800 all their help with single-cell RNA-sequencing experiments, and the University of Birmingham Flow
801 Cytometry Facility. We thank Dr. Y. Miwa (Tsukuba University, Tsukuba, Japan) and Dr. O.
802 Kanagawa (RIKEN Research Center for Allergy and Immunology, Yokohama, Japan) and Dr. M.
803 Tomura (Osaka Ohtani University, Tondabayashi, Japan) for the Kaede mice.

804 **Disclosures**

805 AstraZeneca provided therapeutic anti-PD-L1 antibodies, isotype control antibodies, and MC38-Ova
806 cells. GC, SAH and SJD are full employees and share-holders in AstraZeneca. No other disclosures or
807 conflicts of interest are reported.

808

Figure 1

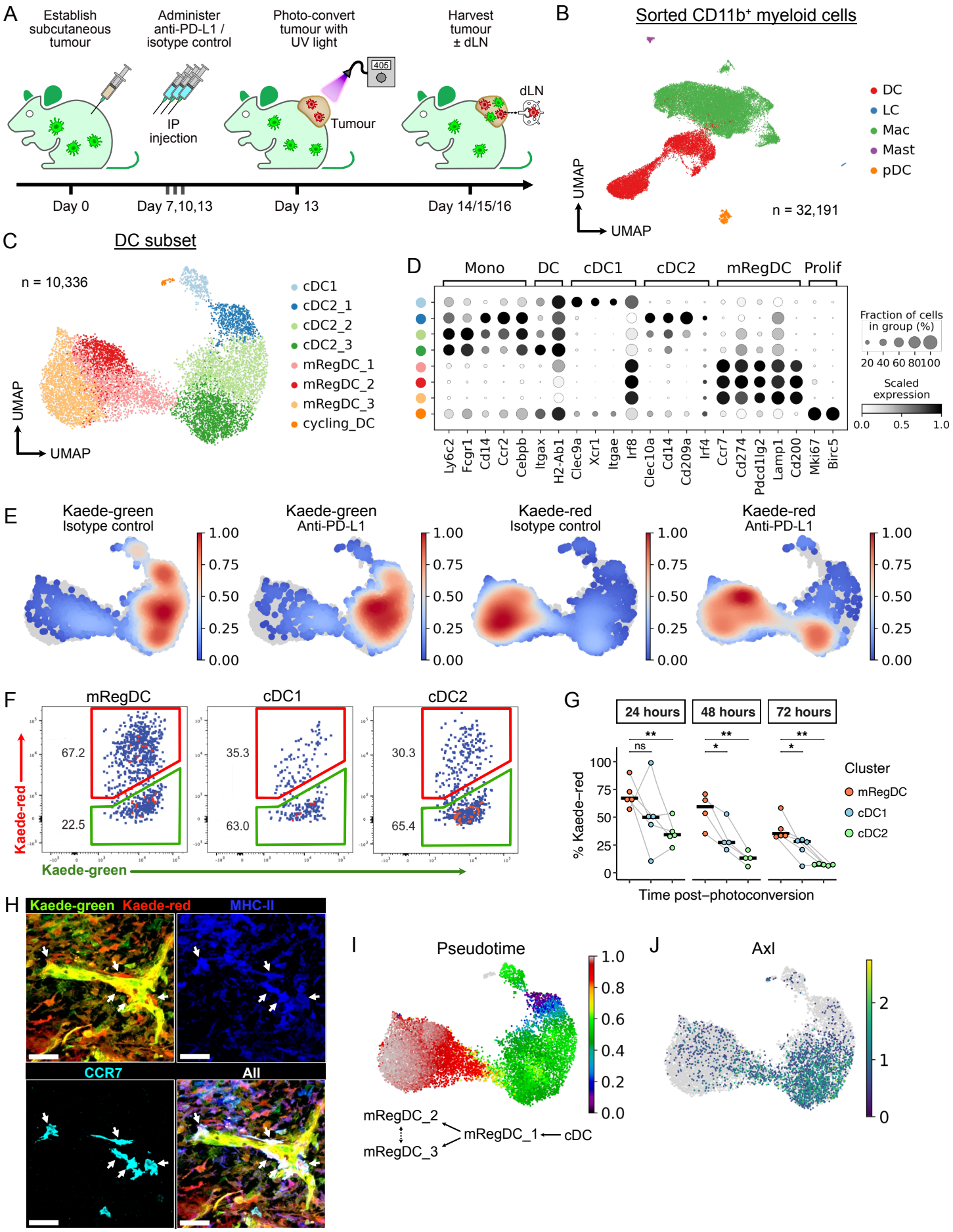
A
Establish subcutaneous tumour
Administer anti-PD-L1 / isotype control
Photo-convert tumour with UV light
Harvest tumour ± dLN
405
IP injection
Tumour
dLN
Day 0
Day 7,10,13
Day 13
Day 14/15/16
B
Sorted CD11b+ myeloid cells
DC
LC
Mac
Mast
pDC
n = 32,191
UMAP
UMAP
C
DC subset
n = 10,336
cDC1
cDC2_1
cDC2_2
cDC2_3
mRegDC_1
mRegDC_2
mRegDC_3
cycling_DC
UMAP
UMAP
D
Mono
DC
cDC1
cDC2
mRegDC
Prolif
Ly6c2
Fcgr1
Cd14
Ccr2
Cebpb
Itgax
H2-Ab1
Clec9a
Xcr1
Itgae
Irf8
Clec10a
Cd14
Cd209a
Irf4
Ccr7
Cd274
Pdcd1lg2
Lamp1
Cd200
Mki67
Birc5
Fraction of cells in group (%)
20 40 60 80100
Scaled expression
0.0 0.5 1.0
E
Kaede-green Isotype control
Kaede-green Anti-PD-L1
Kaede-red Isotype control
Kaede-red Anti-PD-L1
1.00
0.75
0.50
0.25
0.00
F
mRegDC
cDC1
cDC2
67.2
22.5
35.3
63.0
30.3
65.4
Kaede-red
Kaede-green
G
24 hours
48 hours
72 hours
ns
**
*
% Kaede−red
100
75
50
25
0
Cluster
mRegDC
cDC1
cDC2
Time post−photoconversion
H
Kaede-green Kaede-red
MHC-II
CCR7
All
I
Pseudotime
1.0
0.8
0.6
0.4
0.2
0.0
mRegDC_2
mRegDC_3
mRegDC_1
cDC
J
Axl
2
1
0

Figure 1 | Landscape and temporal dynamics of DCs in murine subcutaneous tumours.
(A) Experiment design. Tumours from C57BL/6 Kaede transgenic mice were harvested 24h, 48h, or 72h after photoconversion.
(B) UMAP of 32,191 myeloid cells from scRNA-seq of FACS-sorted $CD45^+CD11b^+$ Kaede-$green^+$/Kaede-red^+ cells 48h after photoconversion of subcutaneous MC38-Ova tumours.
(C) UMAP of 10,336 DCs from (B), and canonical marker gene expression of respective clusters (D).
(E) Density embedding of DCs from each condition (Kaede-green/red, anti-PD-L1/isotype control antibodies).
(F) Representative flow cytometry plots of Kaede-green/red composition in DCs subsets from MC38-Ova tumours 48h post-photoconversion. Data is representative of 3 independent experiments (12 independent mice).
(G) Time-course of DC subsets from MC38-Ova tumours *x* hours after tumour photoconversion. Medians are shown; individual points represent independent mice. Paired student's t-test was used.
(H) Representative confocal microscopy images of CT26 tumours 72h after photoconversion. Scale bar, 40µm; arrows, tumour-residing mRegDCs (Kaede-$red^+CCR7^+MHC\text{-}II^+$, dendritic morphology).
(I) Tumour DCs ordered by pseudotime, rooted in the cluster with highest proportion of Kaede-green DCs.
(J) Expression of *Axl* in tumour DCs.

Figure 2

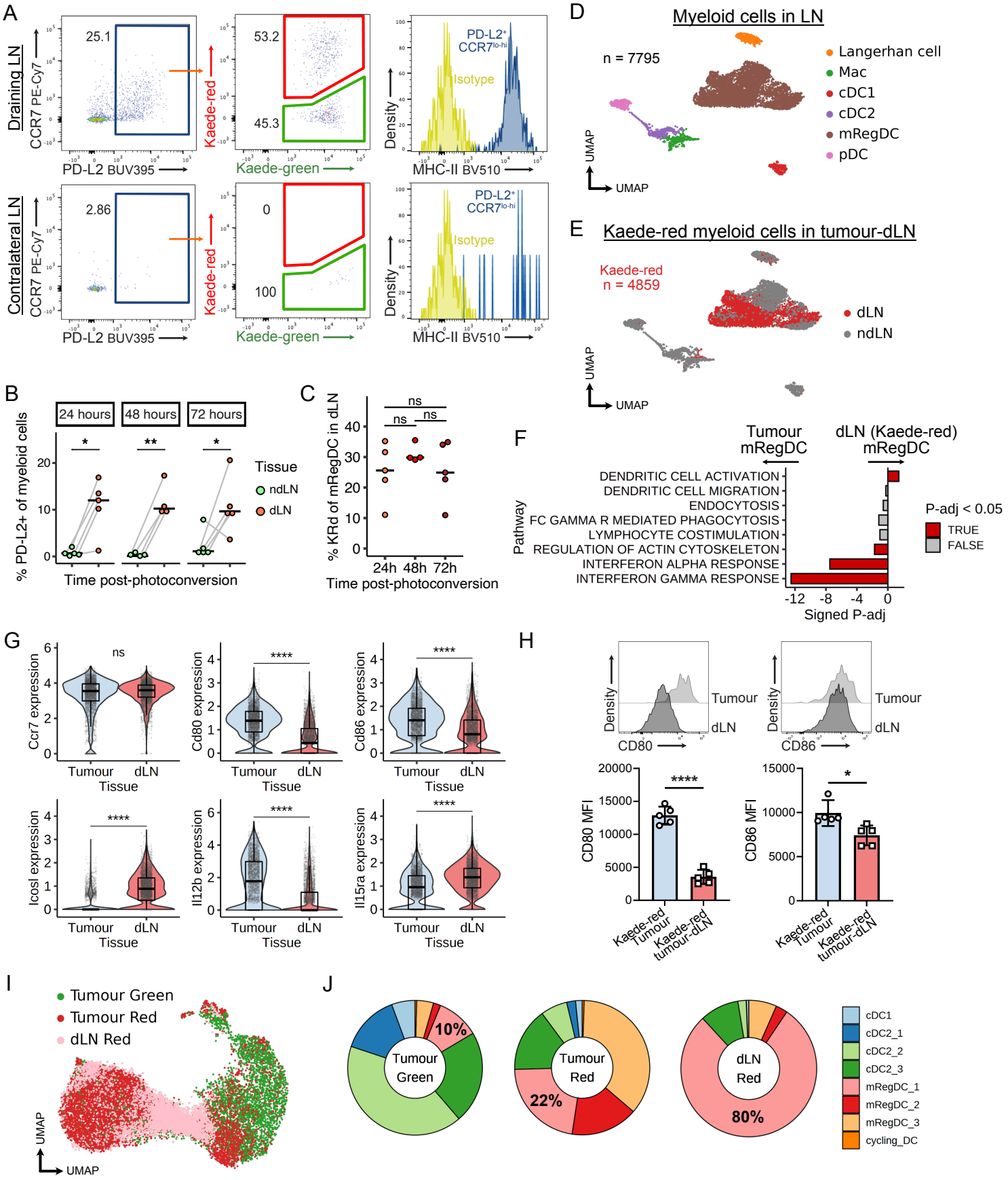
A
Draining LN
Contralateral LN
CCR7 PE-Cy7
PD-L2 BUV395
25.1
2.86
53.2
45.3
0
100
Kaede-red
Kaede-green
PD-L2+ CCR7lo-hi
Isotype
Density
MHC-II BV510
B
24 hours
48 hours
72 hours
% PD-L2+ of myeloid cells
Tissue
ndLN
dLN
Time post-photoconversion
C
% KRd of mRegDC in dLN
ns
24h 48h 72h
Time post-photoconversion
D
Myeloid cells in LN
n = 7795
Langerhan cell
Mac
cDC1
cDC2
mRegDC
pDC
UMAP
E
Kaede-red myeloid cells in tumour-dLN
Kaede-red
n = 4859
dLN
ndLN
F
Tumour mRegDC
dLN (Kaede-red) mRegDC
Pathway
DENDRITIC CELL ACTIVATION
DENDRITIC CELL MIGRATION
ENDOCYTOSIS
FC GAMMA R MEDIATED PHAGOCYTOSIS
LYMPHOCYTE COSTIMULATION
REGULATION OF ACTIN CYTOSKELETON
INTERFERON ALPHA RESPONSE
INTERFERON GAMMA RESPONSE
P-adj < 0.05
TRUE
FALSE
Signed P-adj
G
Ccr7 expression
Cd80 expression
Cd86 expression
Icosl expression
Il12b expression
Il15ra expression
Tumour
dLN
Tissue
H
Density
Tumour
dLN
CD80
CD86
CD80 MFI
CD86 MFI
Kaede-red Tumour
Kaede-red tumour-dLN
I
Tumour Green
Tumour Red
dLN Red
UMAP
J
Tumour Green
Tumour Red
dLN Red
10%
22%
80%
cDC1
cDC2_1
cDC2_2
cDC2_3
mRegDC_1
mRegDC_2
mRegDC_3
cycling_DC

Figure 2 | mRegDCs that migrate to the dLN alter their co-stimulatory phenotype and are transcriptionally distinct from tumour-residing populations.
(A) Representative flow cytometry plots of tumour-dLNs and contralateral ndLNs 48h after tumour photoconversion. DCs that migrate to the LN from photoconverted tumours carry the Kaede-red fluorescent profile, which enables tracking to the dLN.
(B) Time-course of mRegDCs in the dLN versus ndLN *x* hours after tumour photoconversion; and (C) percentage of mRegDCs that are Kaede-red in dLNs. Medians are shown; individual points represent independent mice; paired student's t-test was used.
(D-E) UMAP of 7795 myeloid cells from scRNA-seq of FACS-sorted $CD45^+$ Kaede-red cells from tumour-dLNs and $CD45^+$ cells from control LNs.
(F) GSEA of Kaede-red mRegDCs in the dLN versus mRegDCs in the tumour (isotype control-treated). Signed P-adj indicate $\log_{10}$(adjusted *P*-value) with the direction of the enrichment score.
(G) Expression of selected genes between Kaede-red mRegDCs in the tumour-dLN and mRegDCs in the tumour (isotype control-treated). Wilcoxon rank-sum test was used.
(H) Flow cytometry of surface expression of CD80 and CD86 on mRegDCs 48h after tumour photoconversion. Representative histograms and MFI; means ± standard deviation shown; individual points represent independent mice; Mann-Whitney U test was used.
(I) Integration of Kaede-red DCs from the tumour-dLN with the tumour DC landscape and label transfer.
(J) Proportions of DCs by origin and Kaede profile.

Figure 3

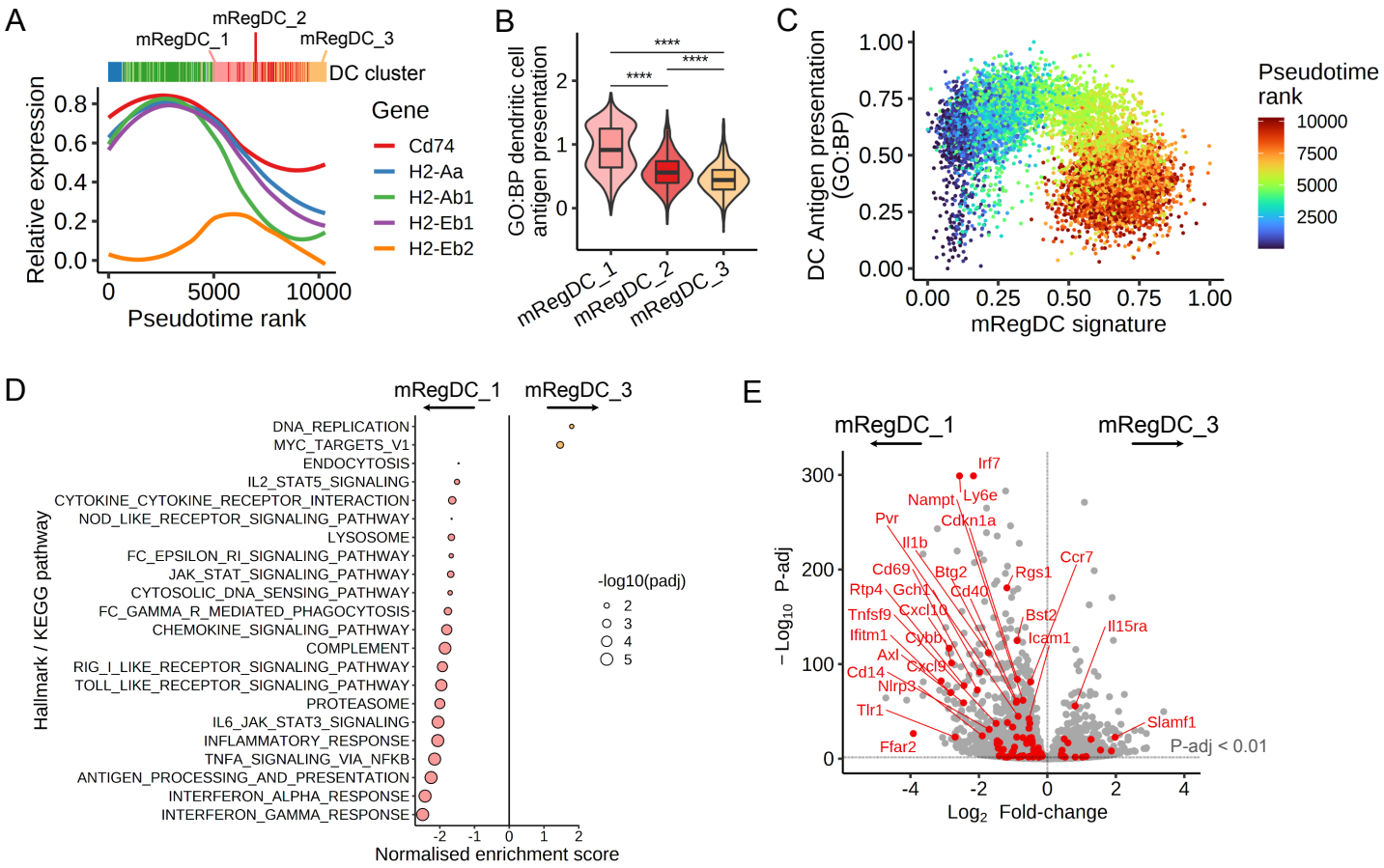

Figure 3 | Tumour-residing mRegDCs undertake an "exhausted" state with duration in the tumour.

(A) Expression of MHC-II transcripts and *Cd74* over pseudotime in tumour DCs. Local polynomial regression (loess) was fit to range-standardised expression values.

(B) Gene signature scores for "*GO:BP dendritic cell antigen processing and presentation (GO:0002468)*" across mRegDC clusters. Wilcoxon rank-sum test was used.

(C) Gene signature scores of individual cells for "*GO:BP dendritic cell antigen processing and presentation (GO:0002468)*" and mRegDC signature genes, coloured by pseudotime. Range-standardised scores shown.

(D) GSEA of mRegDC_3 versus mRegDC_1. Only significantly enriched pathways (*P*-adj < 0.05) shown.

(E) Volcano plot of DEGs between mRegDC_1 and mRegDC_3. Significant DEGs from "*Hallmark inflammatory response*" are highlighted in red (*P*-adj < 0.01).

Figure 4

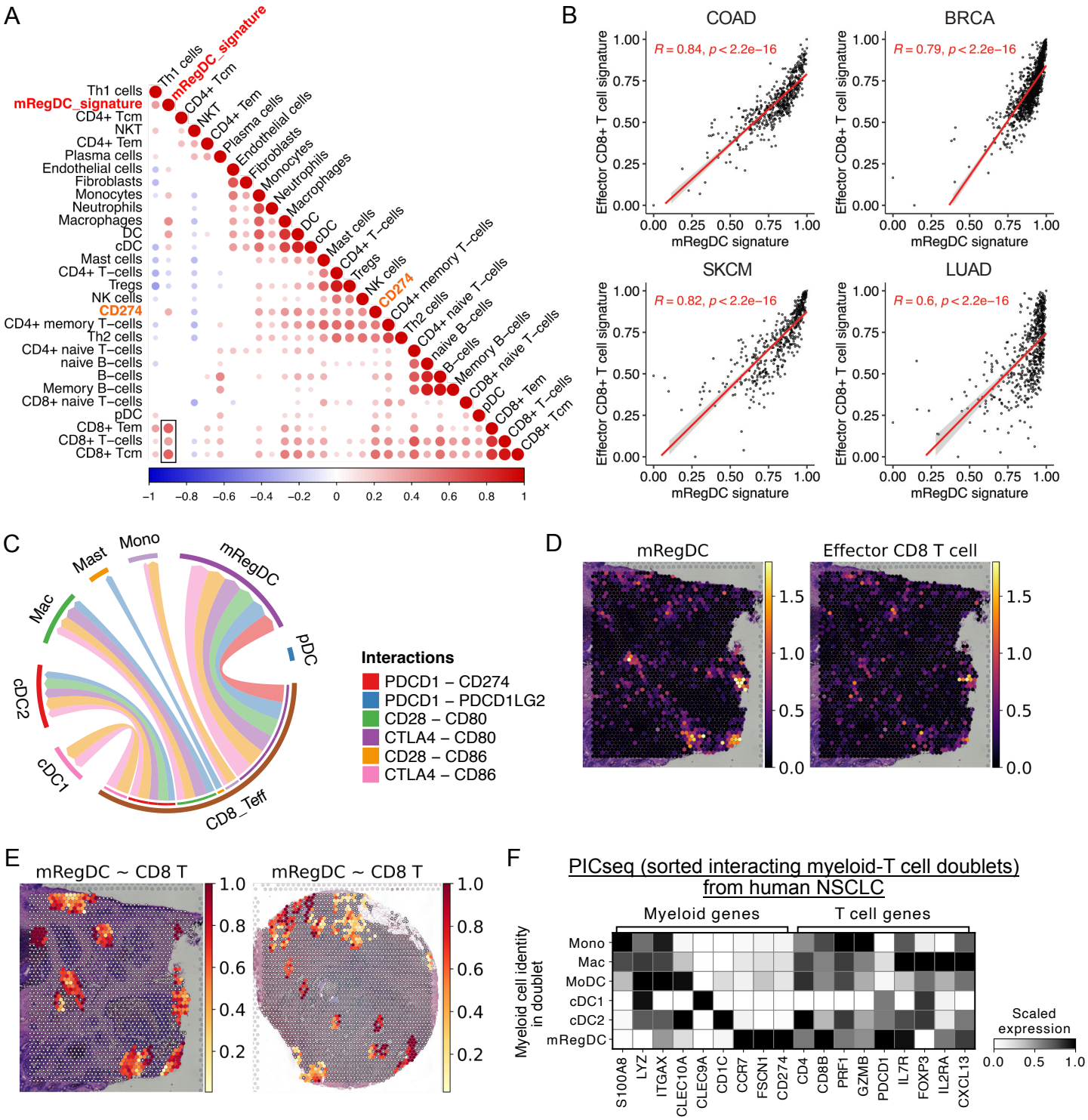

Figure 4 | mRegDCs interact with CD8⁺ T cells in human cancers.
(A) Pearson correlation between cell proportions, from deconvolution of 521 bulk transcriptomes of colorectal adenocarcinoma biopsies (TCGA), and mRegDC signature genes. Box highlights high correlation between mRegDC and CD8⁺ T cells. Only significant correlations ($p < 0.01$) shown.
(B) Pearson correlation between mRegDC signature genes and effector CD8⁺ T cell signature genes in colorectal cancer (COAD), breast cancer (BRCA), cutaneous melanoma (SKCM) and lung adenocarcinoma (LUAD) from TCGA, where enrichment of mRegDC genes shows survival benefit (SFig. 1A).
(C) CellPhoneDB[43] cell-cell communication analysis between myeloid cells and effector CD8⁺ T cells in scRNA-seq of human CRC. Width of edges represent standardised interaction scores. Only significant interactions ($p < 0.01$) shown.
(D) Gene signature scores for mRegDCs and effector CD8⁺ T cells in 10x Visium spatial transcriptomics of a human CRC tumour section.
(E) Spatial correlation of mRegDC and effector CD8⁺ T cell signature scores in spatial transcriptomics of independent human CRC tumour sections ($n = 2$).
(F) Expression of selected genes in myeloid-T cell PICs from NSCLC, grouped by the myeloid cell identity.

Figure 5

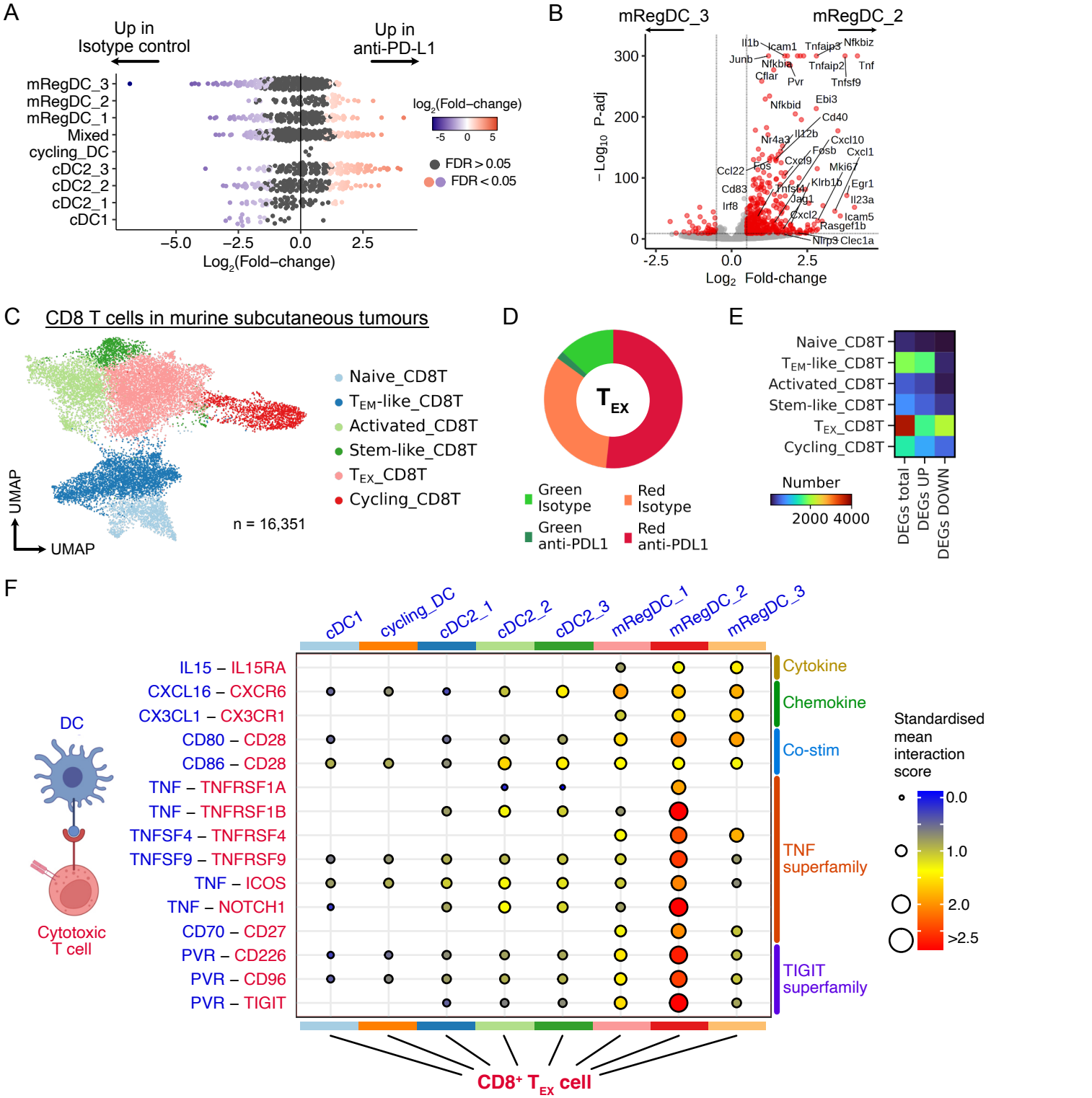
A
Up in Isotype control
Up in anti-PD-L1
mRegDC_3
mRegDC_2
mRegDC_1
Mixed
cycling_DC
cDC2_3
cDC2_2
cDC2_1
cDC1
log2(Fold–change)
FDR > 0.05
FDR < 0.05
Log2(Fold–change)
B
mRegDC_3
mRegDC_2
– Log10 P-adj
Log2 Fold-change
C
CD8 T cells in murine subcutaneous tumours
Naive_CD8T
TEM-like_CD8T
Activated_CD8T
Stem-like_CD8T
TEX_CD8T
Cycling_CD8T
n = 16,351
UMAP
D
TEX
Green Isotype
Red Isotype
Green anti-PDL1
Red anti-PDL1
E
Naive_CD8T
TEM-like_CD8T
Activated_CD8T
Stem-like_CD8T
TEX_CD8T
Cycling_CD8T
Number
DEGs total
DEGs UP
DEGs DOWN
F
cDC1
cycling_DC
cDC2_1
cDC2_2
cDC2_3
mRegDC_1
mRegDC_2
mRegDC_3
IL15 – IL15RA
CXCL16 – CXCR6
CX3CL1 – CX3CR1
CD80 – CD28
CD86 – CD28
TNF – TNFRSF1A
TNF – TNFRSF1B
TNFSF4 – TNFRSF4
TNFSF9 – TNFRSF9
TNF – ICOS
TNF – NOTCH1
CD70 – CD27
PVR – CD226
PVR – CD96
PVR – TIGIT
Cytokine
Chemokine
Co-stim
TNF superfamily
TIGIT superfamily
DC
Cytotoxic T cell
Standardised mean interaction score
CD8+ TEX cell
G
CCR7
MHCII
CD8
CD3
4-1BB
Ki-67
Composite

Figure 5 | anti-PD-L1 promotes activating mRegDC-cytotoxic CD8$^+$ T cell interactions in the TME.

(A) Milo[38] differential abundance analysis of tumour DCs. Bee-swarm plot shows treatment-associated differential abundance in overlapping cellular neighbourhoods (individual points). Differentially abundant neighbourhoods at FDR < 0.05 are coloured. 'Mixed' refers to neighbourhoods where cells do not predominantly (>70%) belong to a single cluster.

(B) Volcano plot between mRegDC_2 and mRegDC_3. DEGs (*P*-adj < 0.01, $\log_2$Fold-change > 0.5) are coloured. Selected genes involved in immune and inflammatory signalling are labelled.

(C) UMAP of cells from scRNA-seq of 16,351 CD8$^+$ T cells, from FACS-sorted CD45$^+$CD11b$^-$ Kaede-green/red TILs 48h after photoconversion of subcutaneous MC38-Ova tumours.

(D) Proportions of CD8$^+$ T_{EX} cells by Kaede profile and treatment.

(E) Number of significant DEGs in anti-PD-L1 versus isotype control-treated tumours. DEGs calculated using Wilcoxon rank-sum test.

(F) CellPhoneDB[43] ligand-receptor interaction analysis between tumour DCs and CD8$^+$ T cells. Only significant interactions ($p < 0.05$) shown.

(G) Representative confocal microscopy images of MC38 tumours, showing co-localisation of CCR7$^+$MHC-II$^+$ mRegDCs and CD3$^+$CD8$^+$4-1BB$^+$Ki-67$^+$ T cells. Scale bar, 20 μm.

Figure 6

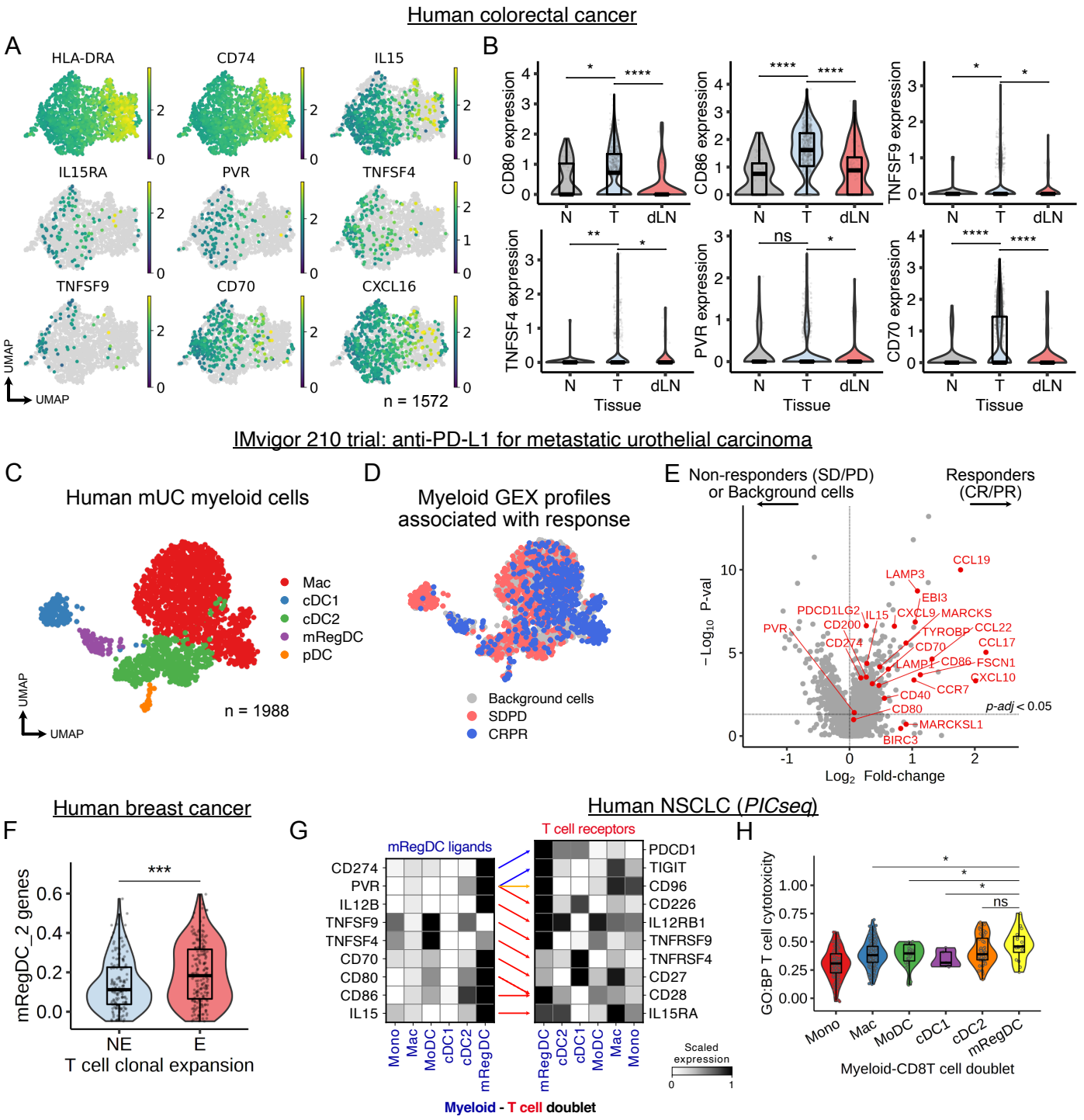
Human colorectal cancer
A
HLA-DRA
CD74
IL15
IL15RA
PVR
TNFSF4
TNFSF9
CD70
CXCL16
UMAP
n = 1572
B
CD80 expression
CD86 expression
TNFSF9 expression
TNFSF4 expression
PVR expression
CD70 expression
N
T
dLN
Tissue
IMvigor 210 trial: anti-PD-L1 for metastatic urothelial carcinoma
C
Human mUC myeloid cells
Mac
cDC1
cDC2
mRegDC
pDC
n = 1988
D
Myeloid GEX profiles associated with response
Background cells
SDPD
CRPR
E
Non-responders (SD/PD) or Background cells
Responders (CR/PR)
CCL19
LAMP3
EBI3
PDCD1LG2
IL15
CXCL9
MARCKS
PVR
CD200
TYROBP
CCL22
CD274
CD70
CCL17
LAMP1
CD86
FSCN1
CXCL10
CCR7
CD40
CD80
p-adj < 0.05
MARCKSL1
BIRC3
−Log10 P-val
Log2 Fold-change
Human breast cancer
F
mRegDC_2 genes
NE
E
T cell clonal expansion
Human NSCLC (PICseq)
G
mRegDC ligands
T cell receptors
CD274
PVR
IL12B
TNFSF9
TNFSF4
CD70
CD80
CD86
IL15
PDCD1
TIGIT
CD96
CD226
IL12RB1
TNFRSF9
TNFRSF4
CD27
CD28
IL15RA
Mono
Mac
MoDC
cDC1
cDC2
mRegDC
Scaled expression
Myeloid - T cell doublet
H
GO:BP T cell cytotoxicity
Myeloid-CD8T cell doublet
Human colorectal cancer (10X Genomics Visium)
I
mRegDC ~ CXCR6
mRegDC ~ TNFRSF4
mRegDC ~ TNFRSF9
mRegDC ~ CD27
mRegDC ~ IL12RB1
mRegDC ~ TIGIT
J

Figure 6 | Conserved mRegDC heterogeneity and CD8$^+$ T cell crosstalk in human cancer.

(A) UMAP of 1572 mRegDCs from human CRC (*n* = 62 patients), from Fig. 1A.

(B) Expression of selected co-stimulatory molecules in mRegDCs between tumour (T), normal adjacent tissue (N) and tumour-dLN, (independent CRC scRNA-seq dataset from (A)[45]). Wilcoxon rank-sum test was used.

(C) UMAP of 1988 myeloid cells from scRNA-seq of human metastatic urothelial carcinoma (mUC, *n* = 11 patients).

(D) Cells associated with response (complete responder, CR; partial responder, PR) or non-responders (stable disease, SD; progressive disease, PD) in the IMvigor 210 trial (atezolizumab) for treatment of mUC. Scissor[50] was used to integrate bulk transcriptomes of patients (*n* = 208) from the IMvigor210 trial and scRNA-seq of myeloid cells from mUC (C).

(E) Volcano plot of gene expression in myeloid cells associated with responders (CR/PR) versus non-responders (SD/PD) from (D).

(F) Gene signature scores for mRegDC_2 transcripts in mRegDCs from human breast cancer treated with anti-PD-1 antibodies. Comparison between T cell clonotype expanders (responders, *n* = 9 patients) versus non-expanders (non-responders, *n* = 20 patients). Wilcoxon rank-sum test was used.

(G) PICseq (myeloid-T cell doublets) of human NSCLC: expression of mRegDC-T cell ligand-receptor pairs, grouped by myeloid cell identity in each myeloid-T cell doublet.

(H) Gene signature scores for "*GO:BP T cell mediated cytotoxicity (GO:0001913)*" (filtered for HLA genes), in myeloid-T cell PICs grouped by the myeloid identity. Wilcoxon rank-sum test was used.

(I-J) Spatial correlation of mRegDC signature scores and selected CD8$^+$ T_{EX} cell receptors, in 10x Visium spatial transcriptomics of 2 independent human CRC tumour sections.

Supplementary Figure 1

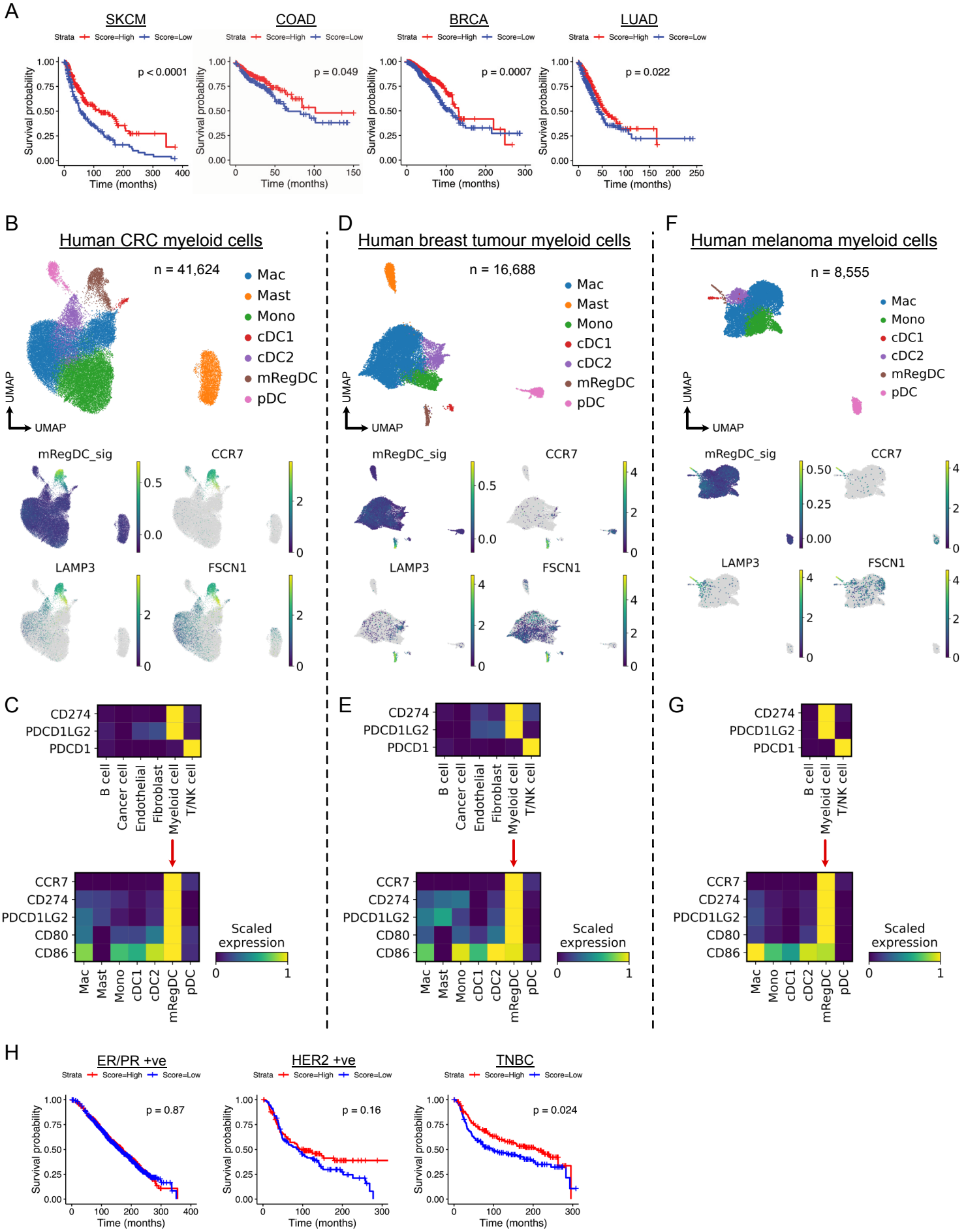

Supplementary Figure 1 | mRegDCs in human cancer.
(A) Kaplan-Meier analysis of overall survival rate in skin cutaneous melanoma (SKCM, n = 473), colorectal adenocarcinoma (COAD, n = 521), breast invasive carcinoma (BRCA, n = 1226), and lung adenocarcinoma (LUAD, n = 598) from TCGA, stratified by enrichment of mRegDC signature genes.
(B) Uniform manifold approximation projection (UMAP) of 41,624 myeloid cells from scRNA-seq of human CRC (n = 62 patients) and expression of mRegDC genes (mRegDC signature score[5], *CCR7*, *LAMP3*, *FSCN1*).
(C) Expression of *CD274* (PD-L1), *PDCD1LG2* (PD-L2) and *PDCD1* (PD-1), *CCR7*, *CD80* and CD86 by cell-type in scRNA-seq of human CRC.
(D) UMAP of 16,688 myeloid cells from scRNA-seq of human breast cancer (n = 29 patients) and expression of mRegDC genes.
(E) Expression of selected genes by cell-type in scRNA-seq of human breast cancer.
(F) UMAP of 8,555 myeloid cells from scRNA-seq of human melanoma (n = 25 patients) and expression of mRegDC genes.
(G) Expression of selected genes by cell-type in scRNA-seq of human melanoma.
(H) Kaplan-Meier analysis of overall survival rate in hormone receptor-positive (oestrogen receptor, ER, or progesterone receptor, PR, n = 1369), human epidermal growth factor receptor 2 (HER2)-positive (n = 185), or triple-negative breast cancer (TNBC, n = 299) from METABRIC. *L*og-rank test was used.

Supplementary Figure 2

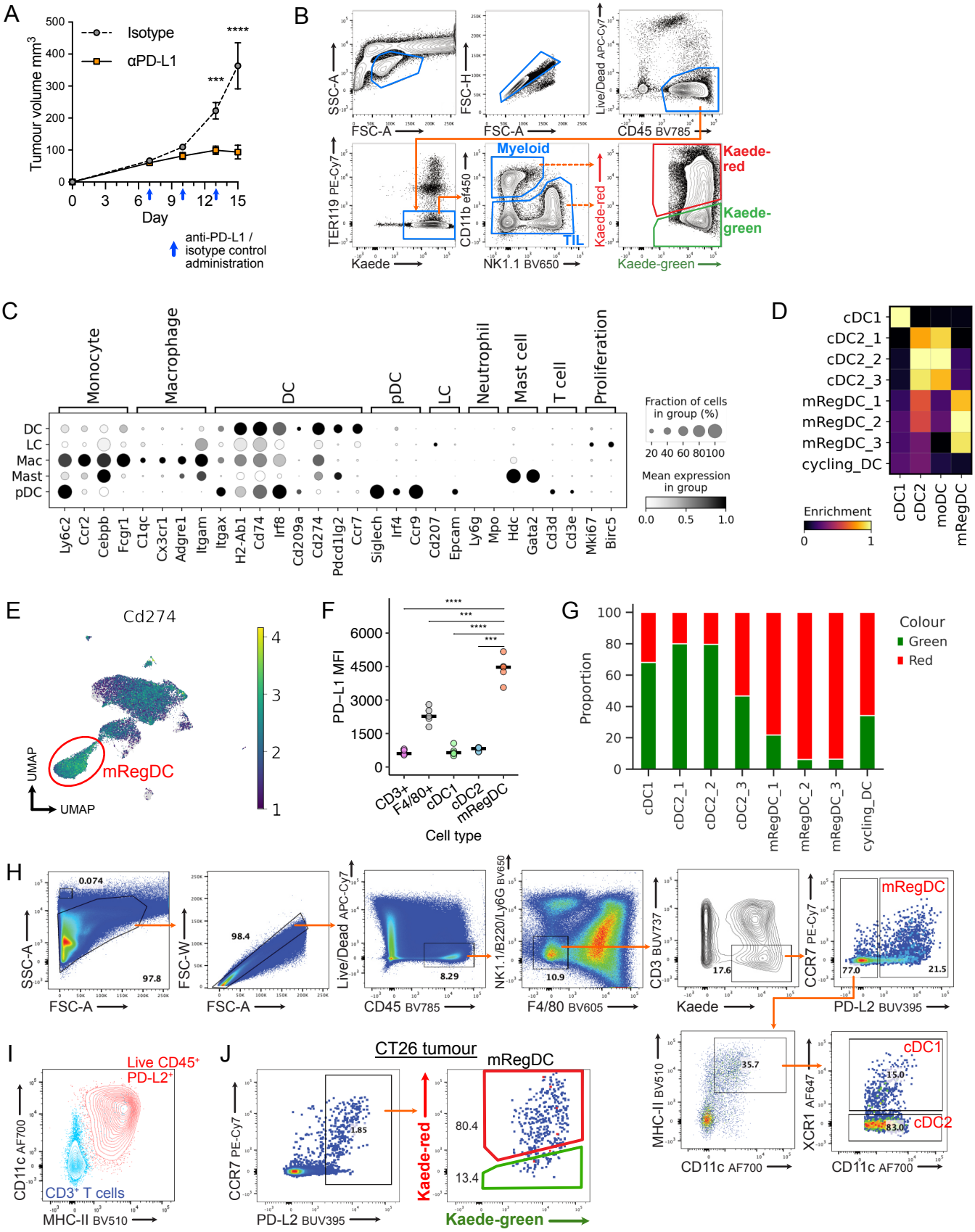

Supplementary Figure 2 | Single cell profiling of mouse subcutaneous tumours.
(A) Tumour growth curves comparing anti-PD-L1 antibody-treated versus isotype control antibody treatment, administered on day 7, 10 and 13, over 15 days. Data shown is related to the scRNA-seq experiment (from Fig. 1) and includes 5 mice per condition.
(B) Fluorescence-activated cell sorting (FACS) strategy for isolation of tumour myeloid cells and TILs, for scRNA-seq.
(C) Canonical marker gene expression in myeloid cell subsets, related to Fig. 2B.
(D) Gene signature scores of published DC transcriptomic signatures in DC clusters from Fig. 2C. Monocyte-derived DCs (moDC) signatures also scored highly in cDC2 clusters, consistent with known challenges in transcriptional distinction of cDC2 and moDC[7].
(E) *Cd274* (PD-L1) expression in myeloid cells.
(F) PD-L1 surface expression of immune cells in MC38-Ova tumours.
(G) Proportion of cells from Kaede-green/red fractions by DC cluster.
(H) Representative flow cytometry gating strategy for identification of tumour DC populations. mRegDCs were identified as Live, $CD45^{+}$ Lin^{-} (NK1.1, B220, Ly6G, CD3, F4/80) $Kaede^{+}$ $PD\text{-}L2^{+}$ $CCR7^{lo\text{-}hi}$ cells. PD-L2 expression was more restricted to mRegDCs than PD-L1 and used as the principal marker to identify mRegDCs.
(I) Representative flow cytometry plot; Live, $CD45^{+}Lin^{-}F/80^{-}CD3^{-}PD\text{-}L2^{+}$ cells are $MHC\text{-}II^{+}$ and $CD11c^{lo\text{-}hi}$, supporting the use of $PD\text{-}L2^{+}$ signal to identify mRegDCs (H). $CD3^{+}$ T cells shown in blue for comparison.
(J) Representative flow cytometry plots of Kaede-green/red composition in mRegDCs from CT26 tumours 48h post-photoconversion. Data is representative of tumours from 6 independent mice.

Supplementary Figure 3

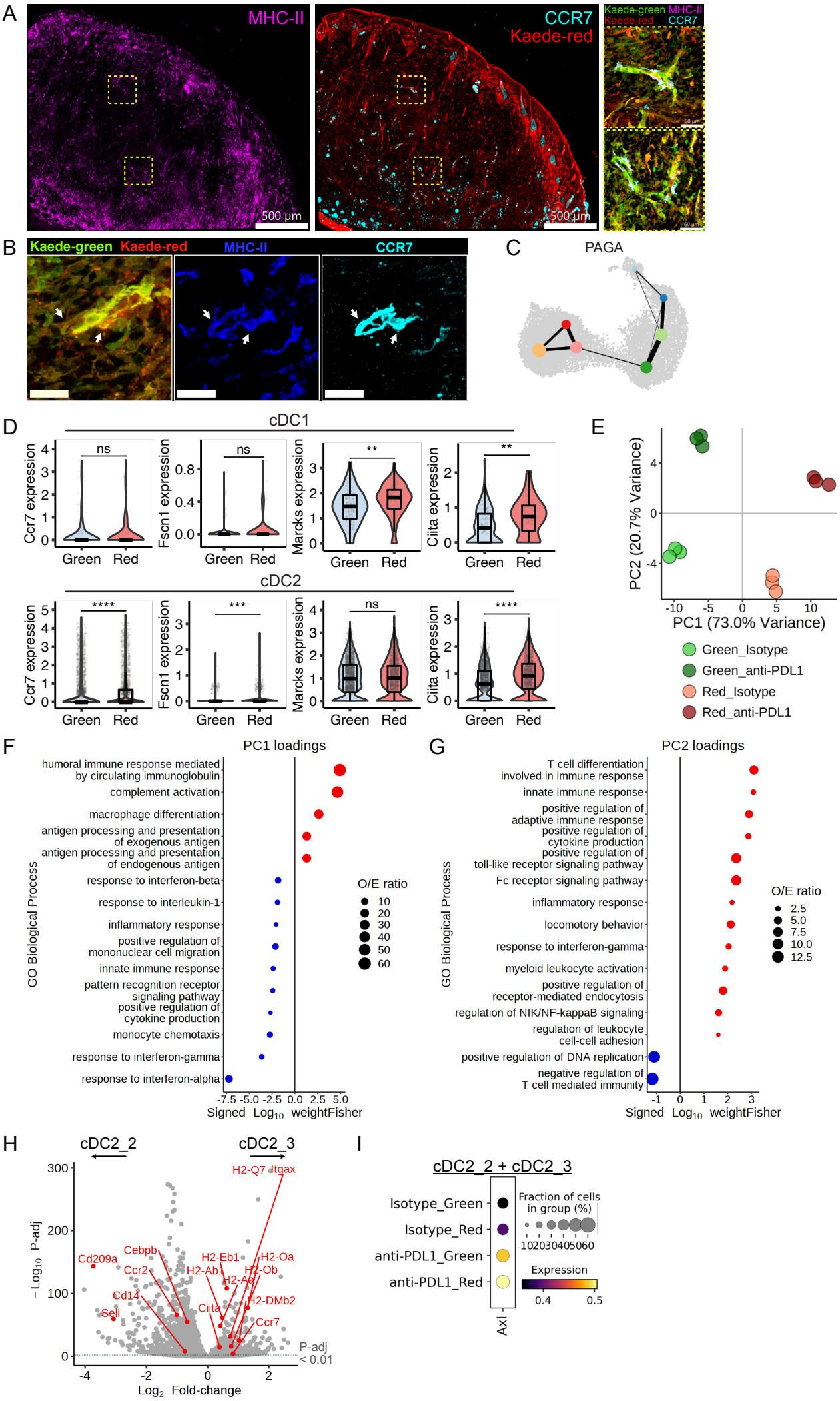

Supplementary Figure 3 | Imaging of tumour mRegDCs and scRNA-seq analysis of pre-mRegDC populations.

(A) Representative confocal microscopy images of CT26 tumours 72h after tumour photoconversion, stained for CCR7 and class-II MHC (MHC-II). Scale bar, 500µm; insets highlight selected regions with $CCR7^{+}MHC\text{-}II^{+}$ DCs.

(B) Representative confocal microscopy images of MC38 tumours 48h after tumour photoconversion. Scale bar, 30µm; arrows, tumour-residing mRegDCs.

(C) Partition-based graph abstraction (PAGA) of scRNA-seq of tumour DC clusters, showing that mRegDC_1 are an intermediate state between cDCs and terminal mRegDC_2/3.

(D) Expression of selected migratory genes and *Ciita* in scRNA-seq data of cDC1 and cDC2, by Kaede profile. Wilcoxon rank-sum test was used.

(E) Principal component (PC) analysis of scRNA-seq of cDC2s, pseudo-bulked to 3 artificial replicates per condition. PC1; variance due to Kaede profile. PC2; variance due to treatment.

(F) Gene ontology (GO) term enrichment test for the top 100 loading genes of PC1 (F) and PC2 (G). O/E, observed/expected ratio; colour, direction of gene loading. Fisher-exact test was used.

(H) Volcano plot of DEGs between cDC2_2 and cDC2_3. Selected DEGs relating to DC maturation, antigen presentation, MHC-II and migration are highlighted in red (all significant, P-adj < 0.01).

(I) Expression of *Axl* in cDC_2 and cDC2_3.

Supplementary Figure 4

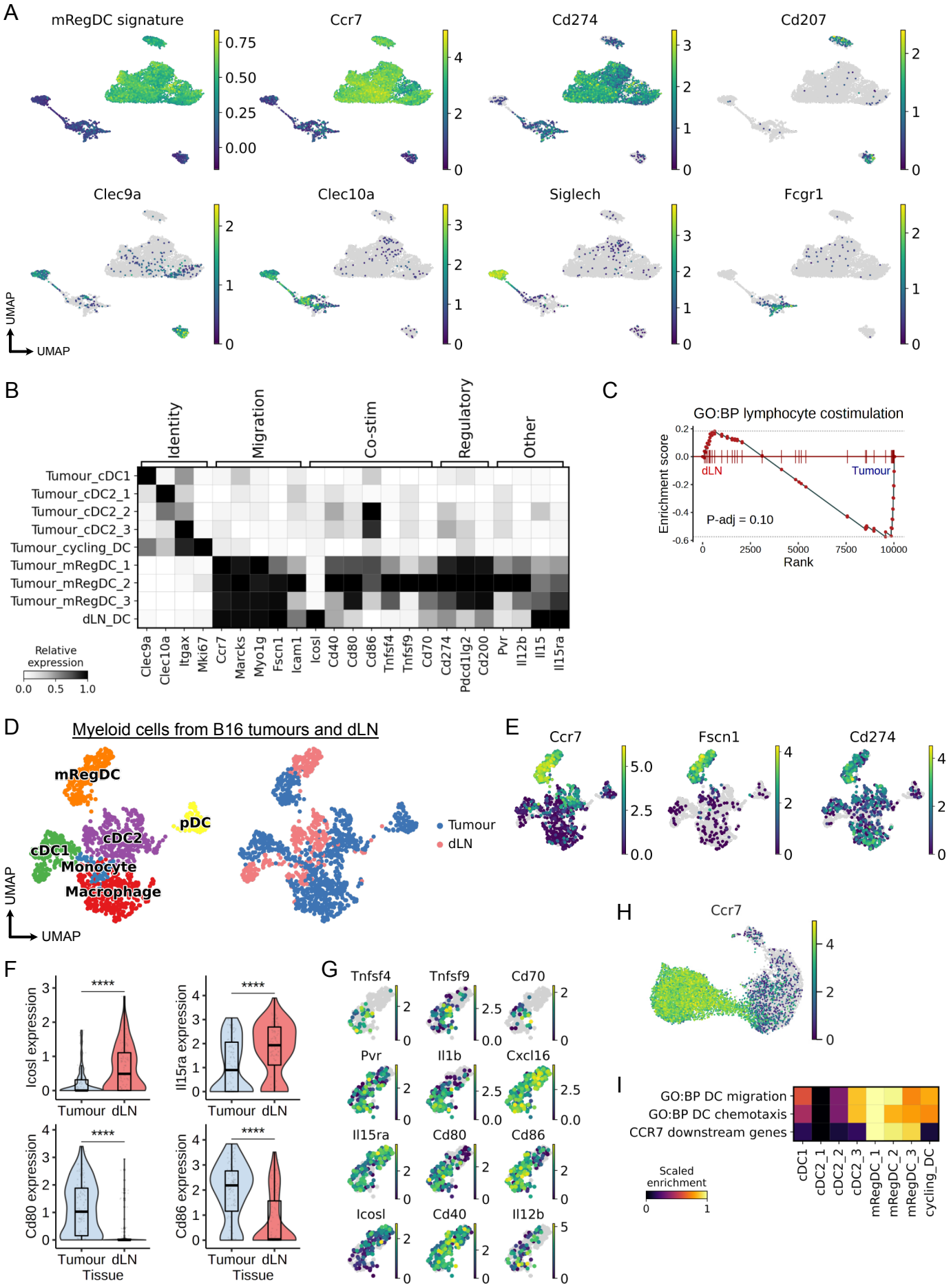

Supplementary Figure 4 | Comparison of mRegDCs in dLNs versus tumour.
(A) Expression of mRegDC or myeloid cell canonical marker genes in LN myeloid cells (Fig. 3C).
(B) Expression of selected genes in DCs from tumours (isotype control-treated) and their tumour-dLNs. DCs from the dLN were most similar to mRegDCs in tumours.
(C) GSEA of "*GO:biological process (BP) lymphocyte co-stimulation (GO:0031294)*", comparing Kaede-red mRegDCs from the dLN versus tumour mRegDCs.
(D) UMAP of 1303 myeloid cells from scRNA-seq of murine subcutaneous B16 tumours and tumour-dLNs, by myeloid cell-type and tissue.
(E) Expression of mRegDC genes.
(F) Expression of selected genes in scRNAseq data of mRegDCs from B16 tumours and tumour-dLNs. Wilcoxon rank-sum test was used.
(G) Expression of additional selected genes in mRegDCs from (D).
(H) Expression of *Ccr7* in DCs from MC38-Ova tumours.
(I) Gene signature enrichment of pathways relating to DC movement and CCR7 signalling.

Supplementary Figure 5

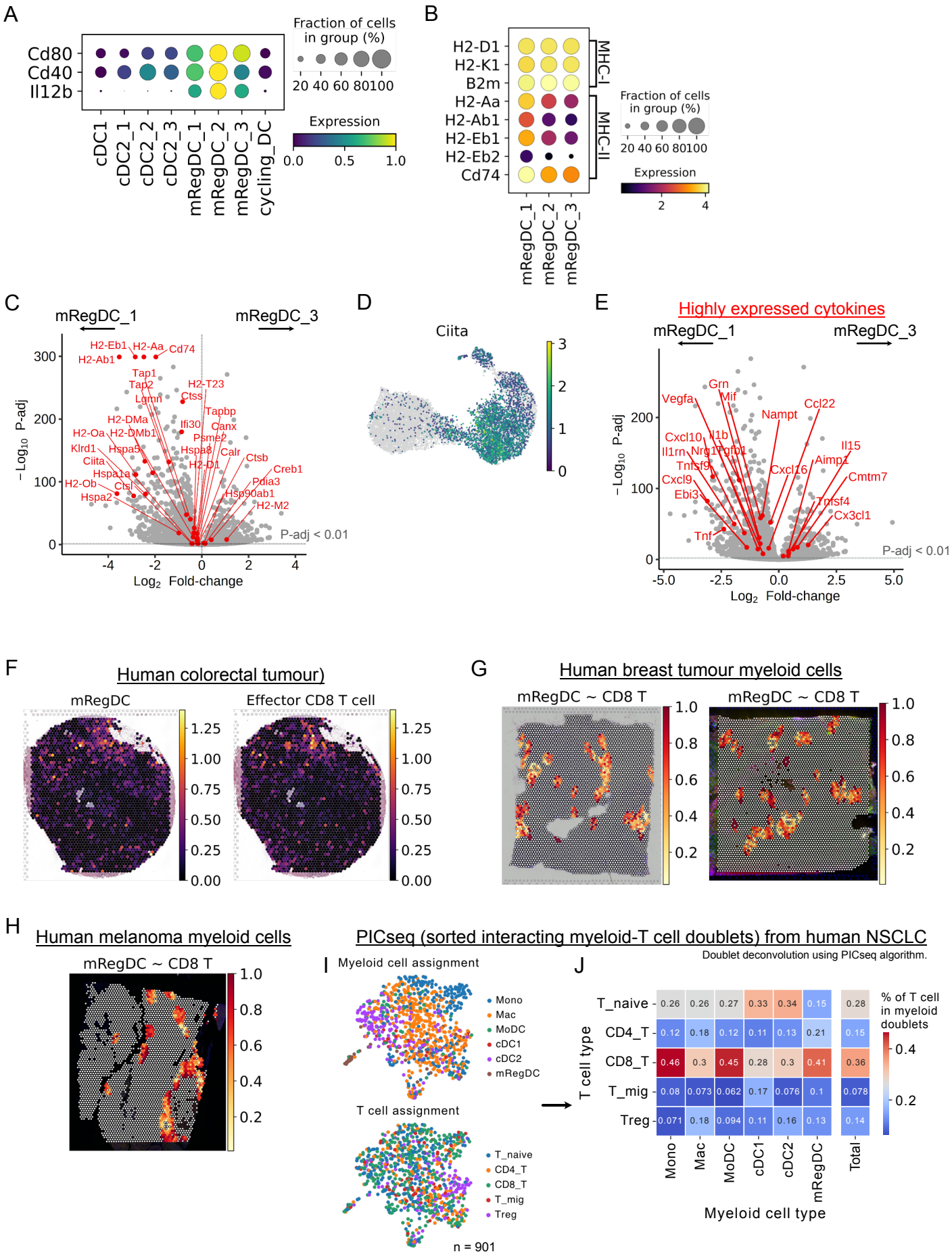

Supplementary Figure 5 | Transcriptional changes in mRegDCs with tumour dwell time and mRegDC CD8$^+$ T cell interactions in human solid tumours.
(A) Dot plot of *Cd80*, *Cd40*, *Il12b* expression in tumour DCs.
(B) Dot plot of class-I and class-II MHC gene expression (log-transformed, unscaled) in mRegDCs.
(C) Volcano plot of DEGs between mRegDC_1 and mRegDC_3. Significant DEGs from "*KEGG antigen processing and presentation*" are highlighted in red (P-adj < 0.01).
(D) Expression of *Ciita* in tumour DCs.
(E) Volcano plot of DEGs between mRegDC_1 and mRegDC_3. Significant DEGs from "*GO: molecular function (MF) cytokine activity (GO:0005125)*" are highlighted in red (P-adj < 0.01).
(F) Gene signature scores for mRegDCs and effector CD8$^+$ T cells in 10x Visium spatial transcriptomics of 1 human CRC tumour section associated with Fig. 4E.
(G) Spatial correlation of mRegDC and effector CD8$^+$ T cell signature scores in spatial transcriptomics of independent human breast tumour sections (n = 2) and a human melanoma section (H, n = 1).
(I) Sequencing of physically interacting cells (PICseq, myeloid-T cell doublets) from human NSCLC (n = 10 patients). UMAP of PICs coloured by the deconvolved myeloid and T cell assignment for each doublet (PICseq algorithm). Each dot represents one myeloid-T cell doublet.
(J) Heatmap of frequency of myeloid-T cell doublet combinations in PICseq of NSCLC.

Supplementary Figure 6

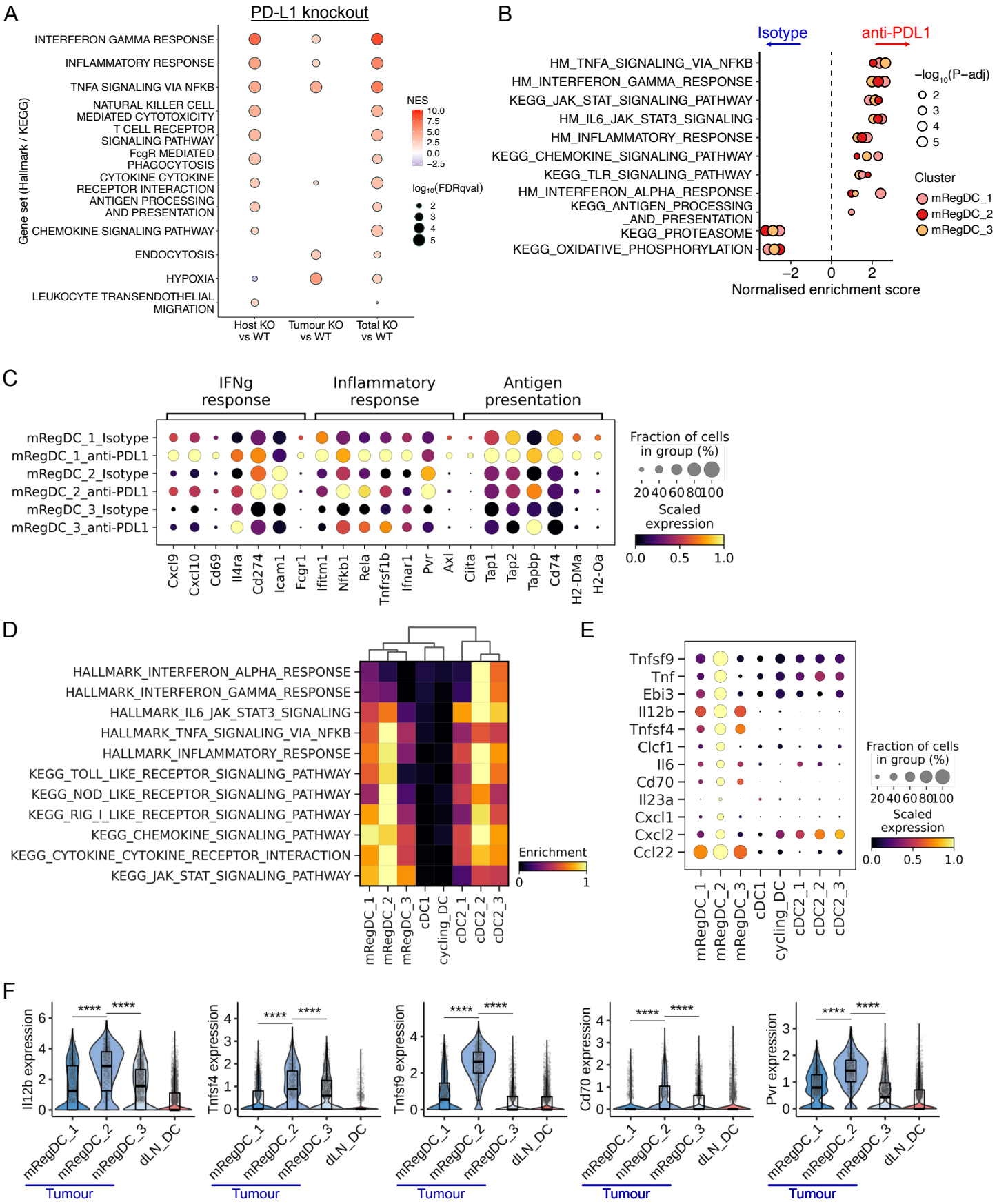

Supplementary Figure 6 | mRegDC activation following anti-PD-L1 treatment.
(A) GSEA of pathways differentially enriched in bulk RNA-seq of PD-L1 knockout (KO) mice injected with wild-type (WT) MC38 tumour cells, WT mice injected with PD-L1 KO tumours, or PD-L1 KO mice injected with PD-L1 KO tumours; versus WT mice injected with WT tumours. Only significant pathways (FDR-q-val < 0.05) are shown; *n=5* biological replicates per condition.
(B) GSEA of mRegDCs by treatment arm in mRegDCs, using Hallmark (HM) and KEGG pathways. Only significant pathways (*P*-adj < 0.05) are shown.
(C) Dot plot of selected leading-edge genes from GSEA analysis of "*Hallmark interferon gamma response*", "*Hallmark inflammatory response*", and "*KEGG antigen processing and presentation*" pathways from (B).
(D) Gene signature scores of selected pathways in mRegDCs.
(E) DEGs in mRegDC_2 versus remaining DC clusters, subset for ligands with cytokine activity (from "*GO:MF cytokine activity (GO:0005125)*"), to identify differentially expressed ligands which may influence the local TME. DEGs calculated using Wilcoxon rank-sum test.
(F) Expression of selected ligands between tumour mRegDC clusters, and Kaede-red DCs that have migrated to the dLN (predominantly mRegDCs, Fig. 2). Wilcoxon rank-sum test was used.

Supplementary Figure 7

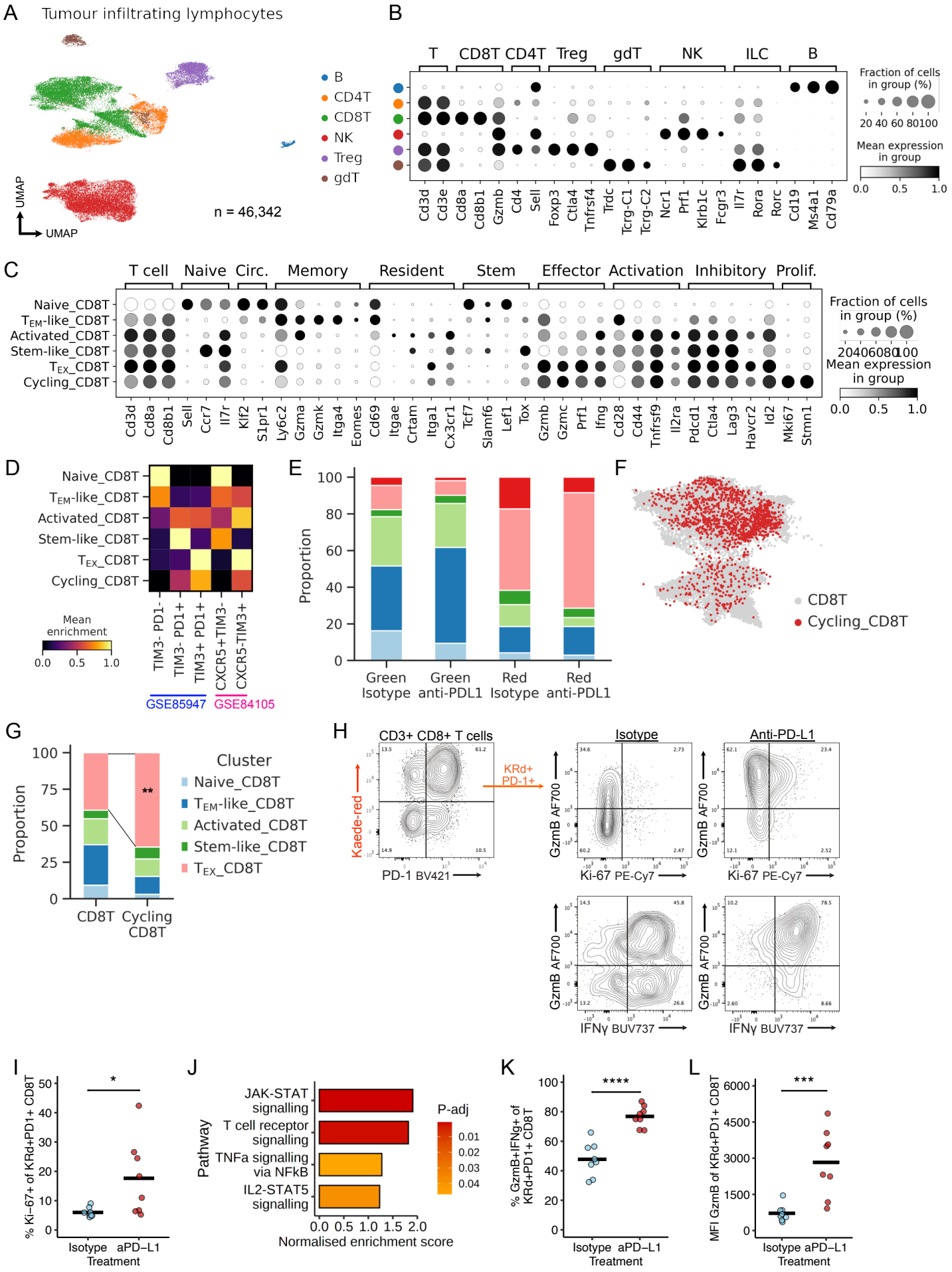

Supplementary Figure 7 | Single cell profiling of tumour CD8$^+$ T cells following anti-PD-L1 treatment.

(A) UMAP of 46,342 T cells from scRNA-seq of FACS-sorted CD45$^+$CD11b$^-$ Kaede-green/red cells 48h after photoconversion of subcutaneous MC38-Ova tumours, representing tumour-infiltrating lymphocytes (TILs), and canonical marker gene expression (B).
(C) Canonical marker gene expression of CD8$^+$ T cell clusters from Fig. 5A.
(D) Gene signature enrichment of published T cell exhaustion transcriptomic signatures in T cell clusters from Fig. 5A.
(E) Proportions of cells by Kaede-green/red and treatment groups in CD8$^+$ T cells.
(F) Regression of cell cycle genes from the cycling_CD8T cluster followed by re-integration, and label transfer. Majority of the cycling cluster embedded with the CD8$^+$ T_{EX} cell cluster.
(G) Proportion of cycling CD8$^+$ T cells belonging to each CD8$^+$ T cell cluster, from (F). Chi-squared test for over-representation of T_{EX} CD8$^+$ T cells was used.
(H) Representative flow cytometry plots of Ki-67$^+$, GzmB$^+$ and IFNγ$^+$ expression in CD3$^+$CD8$^+$Kaede-red$^+$PD-1$^+$ T_{EX} cells, following anti-PD-L1 treatment.
(I) Flow cytometry of Kaede-red$^+$PD-1$^+$CD8$^+$ T cells, showing increased frequency of cycling cells (Ki-67$^+$) following anti-PD-L1.
(J) GSEA for T_{EX} CD8$^+$ T cells from anti-PD-L1 versus isotype control-treated tumours.
(K) Flow cytometry of Kaede-red$^+$PD-1$^+$CD8$^+$ T cells, showing increased frequency of GzmB$^+$IFNγ$^+$ cells following anti-PD-L1.
(L) Flow cytometry of Kaede-red$^+$PD-1$^+$ CD8$^+$ T cells, showing increased mean fluorescence intensity of GzmB following anti-PD-L1. (I, K-L) Points represent independent mice, Mann-Whitney U test was used.

Supplementary Figure 8

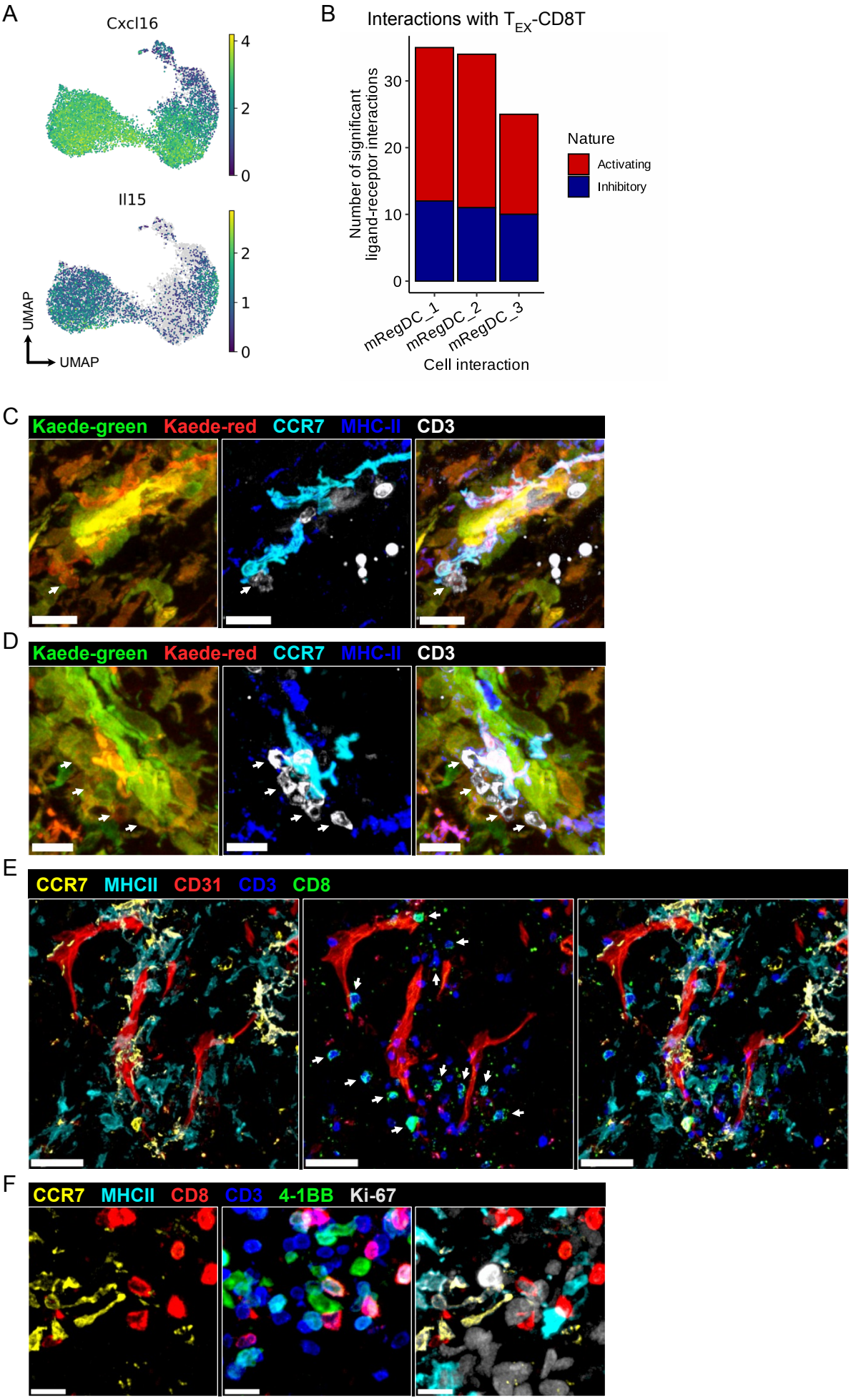

Supplementary Figure 8 | mRegDCs interact with CD8$^+$ T cells in murine tumours.
(A) Expression of *Cxcl16* and *Il15* in tumour DCs.
(B) Number of significant ligand-receptor interactions (from CellPhoneDB), between mRegDC and T_{EX} CD8$^+$ T cells. Interactions that are well-described in existing literature to influence CD8$^+$ T cells function were identified and classified based on whether engagement of the cognate T cell receptor was activating (increase in effector function, proliferation, or survival) or inhibitory in nature.
(C-D) Representative confocal microscopy images of MC38 tumours 48h after tumour photoconversion, showing interaction between Kaede-red CCR7$^+$MHC-II$^+$ mRegDCs and Kaede-red CD3$^+$ T cells (arrows). Scale bar, 20 µm (C), 15 µm (D).
(E) Representative confocal microscopy images of MC38 tumours, showing co-localisation of CCR7$^+$MHC-II$^+$ mRegDCs and CD3$^+$CD8$^+$ T cells (arrows). Scale bar, 80 µm.
(F) Representative confocal microscopy images of MC38 tumours, showing co-localisation of CCR7$^+$MHC-II$^+$ mRegDCs and CD3$^+$CD8$^+$4-1BB$^+$Ki-67$^+$ T cells. Scale bar, 15 µm.

Supplementary Figure 9

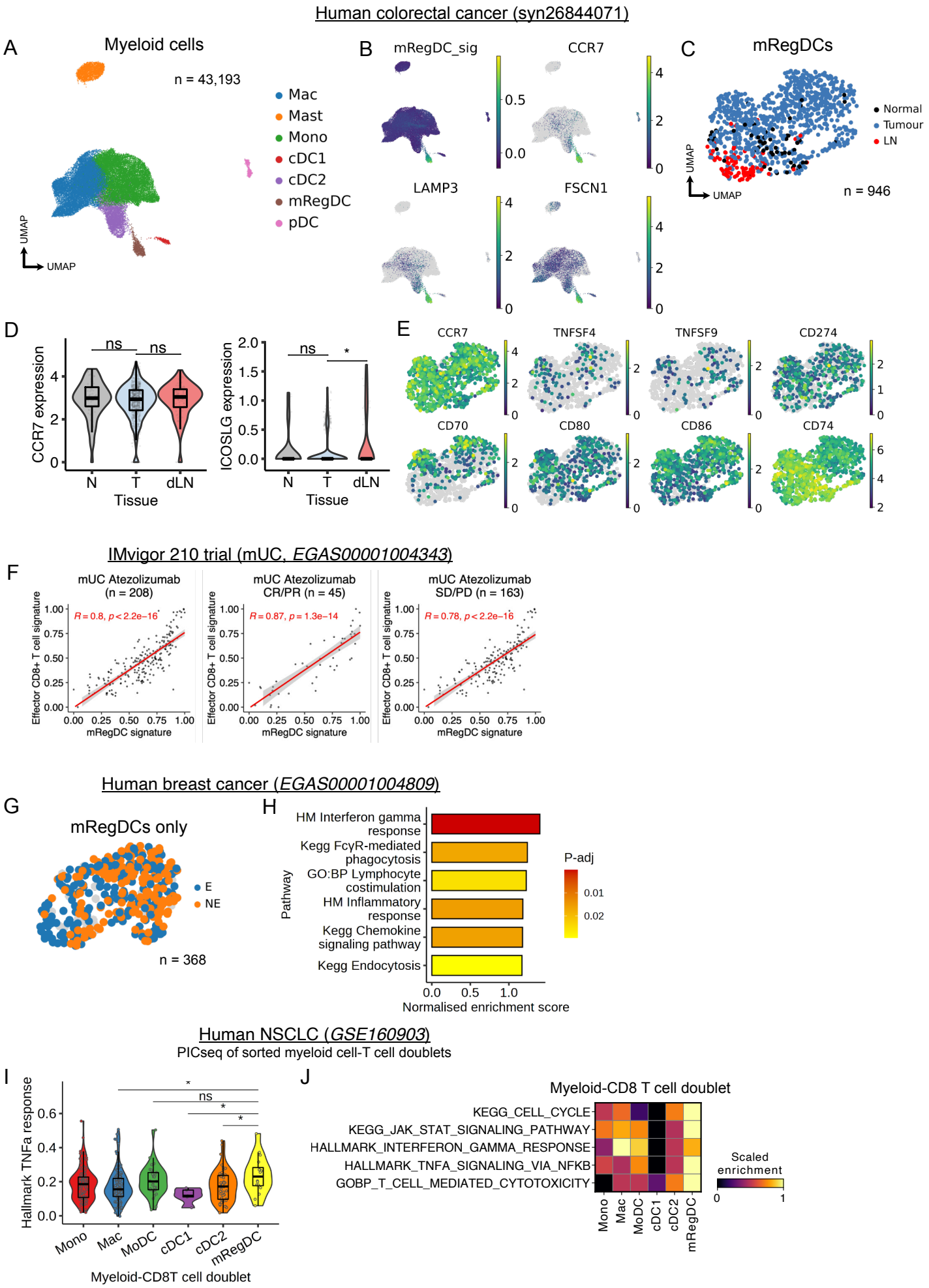

Supplementary Figure 9 | mRegDC heterogeneity and interaction with CD8$^+$ T cells in human cancer.

(A) UMAP of 43,193 myeloid cells from scRNA-seq of human CRC (*n* = 63 patients) with paired tumour (T), dLN and normal adjacent tissue (N), and expression of mRegDC signature genes (B).

(C) UMAP of 946 mRegDCs subsetted from (A), coloured by tissue origin.

(D) Expression of *CCR7* and *ICOSLG* in mRegDCs by tissue. Wilcoxon rank-sum test was used.

(E) Expression of selected genes in mRegDCs from (C). Molecules associated with tumour-residing mRegDCs in mice were selectively expressed in tumour mRegDCs in human CRC, but not the dLN.

(F) Pearson correlation between mRegDC signature genes and effector CD8$^+$ T cell signature genes in bulk RNA-seq of 208 mUC tumours treated with atezolizumab (IMvigor 210 trial). Left, middle and right panel show all patients, clinical responders, and non-responders respectively.

(G) UMAP of 368 mRegDCs from human breast cancer (from Supplementary Fig. 1E).

(H) GSEA of mRegDCs from T cell clonotype expanders (E, i.e. responders, *n* = 9 patients) versus non-expanders (NE, non-responders, *n* = 20 patients), in breast tumours treated with anti-PD-1.

(I) Gene signature score for "*Hallmark TNFa response via NFkB*" in PICseq of NSCLC, grouped by the myeloid cell identity in each myeloid-T cell doublet. Wilcoxon rank-sum test was used.

(J) Gene signature scores of selected pathways in PICs, grouped by the myeloid cell identity.

Supplementary Figure 10

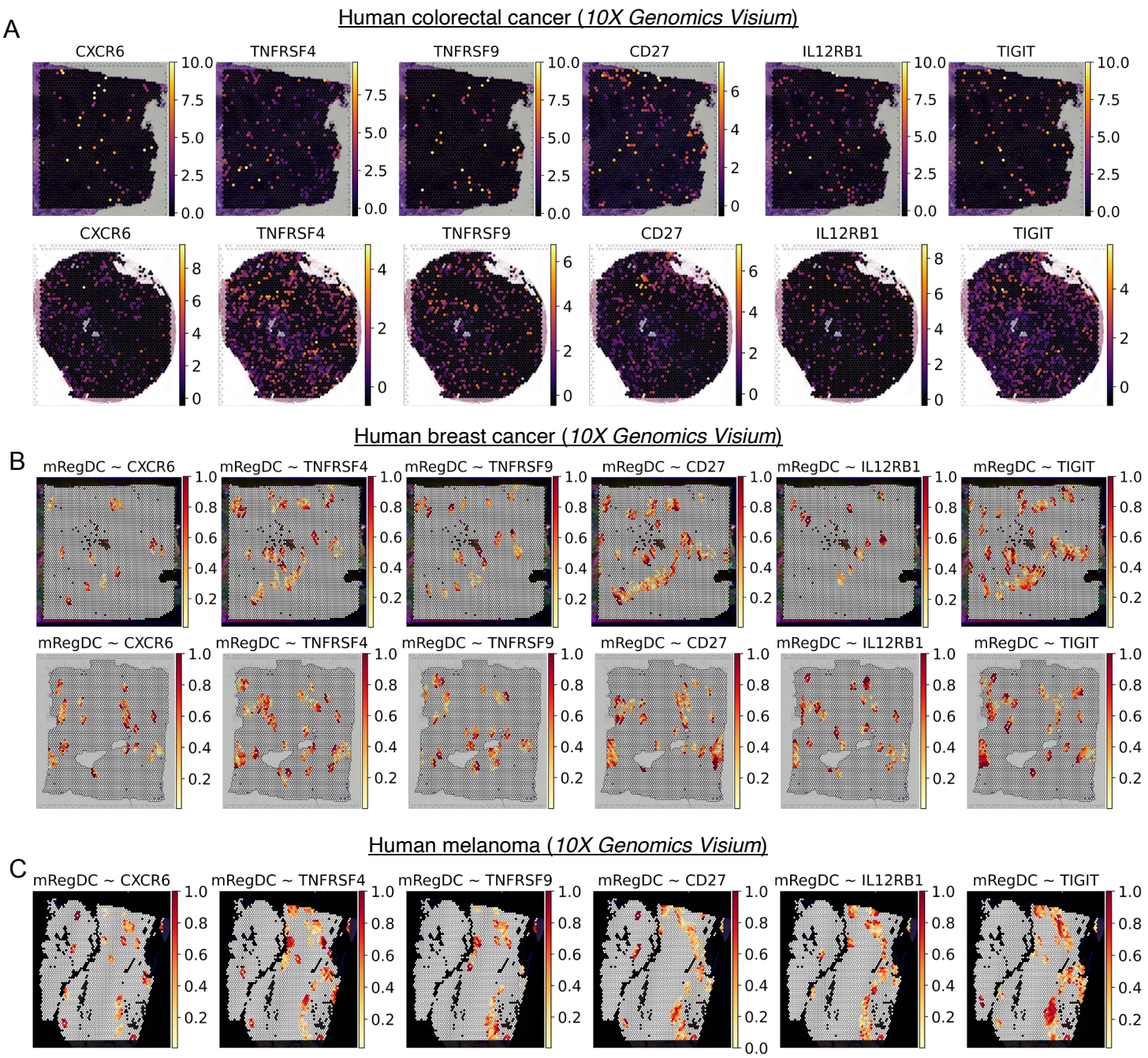

Supplementary Figure 10 | Visium spatial transcriptomics of human cancer.
(A) Expression of selected T_{EX} $CD8^+$ T cell receptors, identified from significant interactions with tumour-residing mRegDCs in spatial transcriptomics of 2 independent human CRC tumour sections.
(B) Spatial correlation of mRegDC signature scores (SFig. 1) and T_{EX} $CD8^+$ T cell receptors of interest, in Visium spatial transcriptomics of 2 independent human breast tumour sections and 1 human melanoma section (C).